Large deformation finite-element modelling of earthquake-induced landslides considering strain-softening behaviour of sensitive clay

Naveel Islam[1], Bipul Hawlader[2*], Chen Wang[3] and Kenichi Soga[4]

[1]Assistant Professor, Department of Civil Engineering, Military Institute of Science and Technology, Bangladesh; formerly Graduate Student, Department of Civil Engineering, Memorial University of Newfoundland, St. John's, Newfoundland and Labrador A1B 3X5, Canada

[2*]**Corresponding Author:** Professor and Research Chair in Seafloor Mechanics, Department of Civil Engineering, Faculty of Engineering and Applied Science**,** Memorial University of Newfoundland, St. John's, Newfoundland and Labrador A1B 3X5, Canada
Tel: +1 (709) 864-8945 Fax: +1 (709) 864-4042 E-mail: bipul@mun.ca

[3]PhD Candidate, Department of Civil Engineering, Faculty of Engineering and Applied Science, Memorial University of Newfoundland, St. John's, Newfoundland and Labrador A1B 3X5, Canada

[4]Chancellor's Professor, Department of Civil and Environmental Engineering, University of California, Berkeley, 447 Davis Hall, Berkeley, California, 94720-1710 USA

Abstract: Large-scale landslides in sensitive clays cannot be explained properly using the traditional limit equilibrium or Lagrangian-based finite-element (FE) methods. In the present study, dynamic FE analysis of sensitive clay slope failures triggered by an earthquake is performed using a large deformation FE modelling technique. A model for post-peak degradation of undrained shear strength as a function of accumulated plastic shear strain (strain-softening) is implemented in FE analysis. The progressive development of "shear bands" (the zone of high plastic shear strains) that causes the failure of a number of soil blocks is successfully simulated. Failure of a slope could occur during an earthquake and also at the post-quake stage until the failed soil masses come to a new static equilibrium. Upslope retrogression and downslope runout of the failed soil blocks are examined for varying geometries and soil properties. The present FE simulations can explain some of the conditions required for causing different types of seismic slope failure (e.g., spread, flowslide or monolithic slides) as observed in the field.

Keywords: sensitive clay slope, retrogressive failure, earthquake, runout, large deformation, flowslide, spread

Introduction

Many large-scale landslides have occurred in sensitive clay slopes (Locat et al. 2011; Thakur 2016). In Canadian sensitive clays, most of the landslides have been triggered by toe erosion and/or human activities. However, earthquakes are the main cause of the largest landslides (Desjardins 1980; Aylsworth and Lawrence 2003; Locat et al. 2011; Brooks 2013; Perret et al. 2013; Demers et al. 2014). Relatively small-scale landslides in sensitive clays were also occurred by earthquakes—for example, the Sainte-Thècle landslide in southern Québec due to the 1988 Saguenay earthquake (Lefebvre et al. 1992). The landslides triggered by toe erosion and human activities have been studied through post-slide investigations and the development of conceptual, analytical and numerical models (Odenstad 1951; Carson 1977, 1979; Quinn 2009; Dey et al. 2015, 2016a). The authors and their co-workers have also presented a review of numerical modelling techniques for large deformation slope failure under static loading (Dey et al. 2015, 2016a–c; Soga et al. 2016).

Empirical relationships have been proposed for assessing large-scale landslides in previous studies (Keefer 1984; Aylsworth and Lawrence 2003; Brooks 2013). Keefer (1984) suggested that a landslide is not expected if the earthquake's magnitude (*M*) is less than 4.0. Reviewing additional failures, the threshold *M* to trigger large landslides in sensitive clays has been found to be between 5.9 and 6.1 (Aylsworth and Lawrence 2003; Brooks 2013). Quinn and Zaleski (2015) attempted to develop relationships between ground acceleration and potential landslides.

Analyzing 41 documented landslides, Mitchell and Markell (1974) categorized six general profiles where slope failures occurred in sensitive clays. In general, flowslides and spreads are the most common types of large-scale seismic landslides (Quinn and Zaleski 2015). However, the development of a large monolithic slab (e.g., Saint Jean-Vianney landslide (Legget and LaSalle

1978)) and formation of deep-seated grabens below the upslope loaded areas (e.g., L-Street slide in the Alaska earthquake (Moriwaki et al. 1985)) have also been reported.

The mechanisms of failure and landslide extent can be examined through physical and numerical modelling. After the Alaska earthquake, small-scale physical model tests were conducted to understand the complex landslide mechanisms (Seed and Wilson 1967). The model slope consisted of an extremely weak clay layer at the level of the toe. In a number of tests, failure was initiated by vibrating the model on a shaking table. Wartman et al. (2005) conducted 1g shaking table tests using a kaolinite–bentonite mixture, which has strain-softening behaviour, to investigate seismic slope displacement. Park and Kutter (2015) presented a series of centrifuge tests where a small amount of Portland cement was mixed with clay to create strain-softening behaviour. One of the main challenges in physical modelling is the accommodation of large displacement of the failed soil mass in a laboratory setup, as typically observed in the field.

The traditional limit equilibrium methods (LEM), which calculate the factor of safety based on a strain-independent soil shear strength, are not suitable for analyzing large-scale landslides in sensitive clays because the LEM cannot model the progressive development of failure planes due to strain-softening. The pseudostatic LEM method, where a destabilizing horizontal body force representing the earthquake-induced force is added to the gravitational driving force, is also not suitable for modeling sensitive clay slope failure, because this method is only applicable if the reduction in shear strength due to earthquake is not very significant (<15%, Seed 1979; Kramer 1996). For a better modelling of this process, Quinn et al. (2012) conducted seismic slope stability analysis decoupling the problem into two components: (i) the progressive development of failure planes has been modeled using the concept of linear elastic fracture mechanics, and (ii) the additional stresses induced by the earthquake have been calculated separately from one-dimensional wave propagation analysis using SHAKE91 (Idriss and Sun 1991).

Dynamic FE modelling of slopes considering post-peak softening of soil is very limited. Kourkoulis et al. (2010) conducted dynamic FE analyses considering linear post-peak degradation of cohesion and frictional soil parameters with accumulated octahedral plastic strains. Chen and Qiu (2014) showed the performance of a smoothed particle hydrodynamics (SPH) method for modelling seismic slope deformation, which has been also calibrated against the shaking table test results of Wartman (1999). However, they did not simulate the retrogression and large displacements of the failed soil blocks, as are observed in seismic landslides in sensitive clays.

Based on an evaluation of historical landslides that occurred in sensitive clays in Québec, Canada, Demers et al. (2014) suggested that there are many factors (e.g. slope geometry, remoulded shear strength, and the thickness of sensitive clay layer) that need to be investigated. Moreover, the methods to analyze progressive slope failure must be improved to understand the characteristics of large retrogressive landslides. The objective of this study is to present large deformation dynamic FE modelling of sensitive clay slope failure in undrained conditions. Total stress analyses have been performed using Abaqus FE software by modelling the soil as an Eulerian material in which the undrained strain-softening behaviour of sensitive clay is implemented. The failure pattern, upslope retrogression and runout of the failed soil mass are investigated by varying the slope geometry and geotechnical properties.

Problem Definition

Numerical analyses are performed for the following four model geometries.

Slope-I: A 15 m high 2H:1V slope with an upslope angle $\alpha = 0°$ is considered (Fig. 1(a)). The downslope profile (ba) is horizontal. However, additional analyses have also been performed for an inclined downslope to investigate its effect on slope failure, especially runout. A large soil domain of 400-m length, having left and right boundaries at 150 m and 250 m, respectively, from the toe, is modelled to minimize boundary effects on slope failure. The soil domain consists of two clay layers and a strong base layer. The groundwater table is located at the ground surface (e.g. the soil is fully saturated). In the field, a weathered crust of variable thickness generally exists over the sensitive clay layer. The behaviour of the crust cannot be modelled properly using the undrained shear strength (Dey et al. 2015). In the present study, the crust is not modelled.

Slope-II: This slope is same as the Slope-I, except for $\alpha>0°$ (Fig. 1(b)).

Slope-III: This slope is also same as Slope-I; however, a vertical surcharge (q) exists in the upslope area, which represents the pressure from existing structures such as buildings or embankments (Fig. 1(c)).

Slope-IV: The geometry of this slope is the same as for Slope-I; however, a weak and highly sensitive clay layer of thickness H_q is placed above the level of the toe (Fig. 1(d)).

FE Modeling

Previous studies showed the advantages of FE modelling over traditional limit equilibrium methods for slope stability analysis (Duncan 1996; Griffiths and Lane 1999). The main advantages of FE modeling are: (i) a priori definition of a failure plane is not required as with LEM; instead, the failure occurs through the location where shear stress reaches the shear strength; (ii) the progressive formation of failure planes can be simulated; and (iii) the deformation of failed soil can be modelled. Large deformation of the failed soil mass occurs in many sensitive clay slope failures. However, most existing FE programs developed in the Lagrangian framework cannot simulate large deformation because of significant mesh distortions around the failure plane that cause numerical instabilities and non-convergences of the solutions (Griffiths and Lane 1999). In the present study, Abaqus/Explicit Version 6.14.2 FE software is used for numerical analysis. The soil is modelled as an Eulerian material to simulate the large deformation of failed soil in a landslide. Note that, unlike the approaches used for modeling Eulerian materials in typical Computational Fluid Dynamics (CFD) programs (including Abaqus CFD), the Eulerian time integration in Abaqus FE program is performed in the Computational Solid Mechanics framework based on operator splitting of the governing equations in which each of the time steps has two phases of calculations—a conventional Lagrangian phase followed by an Eulerian phase. In the Eulerian phase, the solution obtained from the Lagrangian phase is mapped back to the spatially fixed Eulerian mesh. Therefore, the Eulerian material (soil) can flow through the fixed mesh without causing numerical issues related to mesh distortion. Further details of the mathematical formulations, the interactions between the Eulerian material and Lagrangian bodies based on the Coupled Eulerian-Lagrangian (CEL) approach and its applications to large deformation static/quasi-static problems (e.g. onshore and offshore landslides, penetration of surface laid pipelines and pile jacking) are available in previous studies (Benson 1992; Benson and Okazawa 2004; Qiu et al. 2011; Dey et al. 2015, 2016c; Dutta et al. 2015; Trapper et al. 2015).

FE analysis is performed with only one element length in the out-of-plane direction in order to simulate the plane strain condition. A large rectangular Eulerian domain is created first (e.g. PQRS in Fig. 1(a)), which is then discretized using 8-node linear brick elements of multimaterials having reduced integration with hourglass control (EC3D8R in Abaqus) of 0.25 m length, except for the mesh sensitivity analyses. The domain is then divided into two parts: (i) the soil (below abcd in Fig 1(a)) and (ii) the void above the soil layer. The void space is created in order to accommodate the displaced soil mass during the landslide. The initial condition is defined using Eulerian Volume Fraction (EVF). For an element, EVF = 1 means that the element is filled with soil and EVF = 0 means the element is void. A fractional value of EVF means that the element is partially filled with the soil. The density of saturated soil is assigned to all the soil elements.

Zero velocity boundary conditions are applied normal to the bottom and two out-of-planes (i.e. vertical planes parallel to the model) in Fig. 1. In other words, the bottom of the model is restrained from any vertical movement while these vertical faces are restrained from any lateral movement. No boundary conditions are applied along the soil-void interface, to allow the displaced soil to move in the void space when needed. Non-reflecting boundary conditions are applied to the left and right vertical faces in order to avoid reflection of waves during dynamic loading. The advantages of non-reflecting boundary conditions have been discussed elsewhere (Islam 2017; Islam et al. 2017).

FE modelling consists of the following steps.

(i) Gravity loading: The gravitational acceleration (g) is applied gradually to create geostatic stresses in the soil elements, maintaining a ratio between the lateral and vertical total stresses equal to 1.0. This also represents the at-rest earth pressure coefficient (K_0) equal to 1.0 because the pore water pressure is isotropic. The gravitational loading creates shear stress in the soil elements near the slope; however, it is less than the shear strength of soil and therefore the slope is stable at the end of this loading step for the cases analyzed. A wide variation in K_0 for sensitive clays has been reported from field and laboratory measurements, which can be related to the over-consolidation ratio (OCR) as $K_0 = K_{0(NC)}OCR^n$ where $K_{0(NC)}$ is the value of K_0 at the normally consolidated state and $n \sim 1.0$ for Canadian sensitive clays, which could be higher for highly sensitive clays (Lefebvre et al. 1991; Hamouche et al.

1995). K_0 has a significant influence on slope failure (Lo and Lee 1973; Locat et al. 2013; Wang et al. 2015) and therefore further investigation for varying K_0 is required. Moreover, groundwater seepage could influence the initiation of slope failure; however, it has not been modelled in the present study.

For Slope-III, the vertical pressure q is created by increasing the unit weight of a soil block of 20 m width and 0.25 m depth (one element) at the loaded area (Fig. 1(c)).

(ii) Earthquake loading: A horizontal excitation (acceleration–time) is applied at the base of the model (e.g. at PQ in Fig. 1(a)).

(iii) Post-quake simulation: After the completion of earthquake loading, the analysis is continued until the instantaneous velocity of the soil elements becomes negligible.

Figure 2 shows the input acceleration–time history used in this study, which is a modified form of the 1985 Nahanni earthquake that occurred in the Northwest Territories in Canada (Wetmiller et al. 1988; PEER 2010). The modification is performed by multiplying acceleration and the time of the original accelerogram record by scale factors (Villaverde 2009) and, in this case, these factors are 2.0 for acceleration and 1.0 for time. The simulations are conducted in total stress undrained conditions and any post-earthquake pore water migration is not modelled.

Modelling of Soil

An appropriate stress–strain model of sensitive clays that covers a wide range of strains under dynamic and monotonic loadings in undrained conditions is required for successful simulation of slope failures during the earthquake and post-quake phases. The soil is modelled as elastic-plastic material, based on the von Mises yield criterion in total stress analysis. The stress–strain behaviour up to the peak undrained shear strength is considered as linear elastic and defined by undrained Young's modulus (E_u) and Poisson's ratio (ν_u).

Most of the existing laboratory tests available in the literature, such as dynamic triaxial or direct simple shear (DSS) tests, were conducted to investigate the stress–strain behaviour of clays at low to medium strain ranges, or above a threshold deviatoric stress but below the peak shear strength, to model strength degradation of clays with dynamic loading. Díaz-Rodríguez and López-Molina (2008) divided the available studies on the dynamic behaviour of clays into a number of groups based on strain level and showed that experimental studies at large strains are not available. One of the main reasons is that triaxial and DSS devices cannot handle very large deformations.

During the failure of a sensitive clay slope, significantly large strains generate, especially near the failure planes. Recognizing the limitations of typical shear test apparatus for large strain tests, Tavenas et al. (1983) conducted four different types of test—impact on a rigid surface, impact from falling objects, extrusion through a narrowing tube, and shear reversals in a large shear box—on the Champlain sea clays from 7 different sites in Quebec, Canada and showed the degradation of mobilized undrained shear strength (s_u) with strain energy. Quinn et al. (2011) reexamined Tavenas et al.'s (1983) test results and presented s_u degradation as a function of shear displacement. Thakur et al. (2017) showed the post-peak reduction of undrained shear strength with vane rotation.

A very limited number of experimental studies on s_u degradation of sensitive clays under dynamic loading is available in the literature (Lefebvre and LeBoeuf 1987; Kakoli 2005; Javed 2011; Rasmussen 2012; Theenathayarl 2015). In these tests, loading/unloading occurs at stresses below the peak s_u. However, Theenathayarl (2015) showed a large s_u reduction per cycle for stress reversal at strains after the mobilization of the peak s_u with large strain amplitudes.

Post-Peak Shear Strength Degradation

Figure 3 shows the variation of mobilized undrained shear strength (s_u) of sensitive clay with accumulated plastic shear displacement (δ_t). The shear strain localizes into the shear band during strain-softening; therefore, it has been preferred to model the shear strength variation with shear displacement, as is commonly used for modelling shear band propagation based on the concept of fracture mechanics (e.g., Palmer and Rice 1973). The degradation of s_u occurs if $\delta_t > \delta_e + \delta_{pc}$, where δ_e represents the elastic shear displacement and δ_{pc} is the plastic shear displacement during which s_u remains constant. For brevity, the plastic shear displacement in the strain-softening phase is termed as δ (= $\delta_t - (\delta_e + \delta_{pc})$).

When an unloading occurs (e.g., during an earthquake) from a point on the post-peak degradation curve (δ>0), the maximum s_u for the load reversal is equal to the s_u that mobilized before reversal. When the shear stress during the load reversal reaches this s_u, plastic shear strain generates that also causes s_u degradation. In other words, δ in Fig. 3 represents the accumulated plastic shear displacements that occurred in both the loading and unloading phases. Moreover, δ is related to plastic shear strain, as discussed later.

The initial peak undrained shear strength (s_{u0}) remains constant up to δ_{pc}. The shear strength decreases quickly after δ_{pc}, which is primarily due to the collapse of the structure of sensitive clay. At a very large strain, remoulding of soil together with reorientation of particles reduce s_u to the residual shear strength (s_{ur}), as observed from a close examination of soil after vane shear tests (Gylland et al. 2013). Bernander (2000) suggested that s_{ur} does not generally mobilize in a developing slip surface and therefore recommended an undrained shear strength s_{uR} (>s_{ur}) for modelling progressive failure of sensitive clay slopes.

The first segment of the s_u degradation curve (bcd in Fig. 3) (e.g. $0 \leq \delta \leq 2\delta_{95}$) is modelled as

(1) $$s_u = s_{uR} + (s_{u0} - s_{uR})e^{-3\delta/\delta_{95}}$$

where s_{uR} is the value of s_u at large δ; and δ_{95} is the value of δ at which 95% reduction of (s_{u0}-s_{uR}) occurs. Equation (1) is a modified form of the strength degradation equation proposed by Einav and Randolph (2005), but in terms of plastic shear displacement. Note that a linear degradation of s_u with accumulated shear strains during cyclic loading has been used in previous studies (Nadim 1998; Pestana and Nadim 2000). Equation (1) has also been used for modelling T-bar/ball/offshore pipelines subjected to monotonic and cyclic loadings (Zhou and Randolph 2009; Dutta et al. 2015), and large-scale landslides (Wang et al. 2013; Dey et al. 2015). Further details, including the calibration of Eq. (1) against laboratory test results, are available in Dey et al. (2016b).

As shown in the following sections of this paper, s_u at very large strains influences the mobility of the failed soil (e.g. runout) and thereby the failure patterns. A linear variation of s_u with δ is used for the second segment of the strain-softening curve (de in Fig. 3) (e.g. $2\delta_{95} \le \delta \le \delta_{ld}$). Here, δ_{ld} represents a very large plastic shear displacement beyond which s_u remains constant (= $s_{u(ld)}$). Monotonic and cyclic triaxial and direct simple shear tests on sensitive clays show that s_{u0} increases with strain rate but decreases with cyclic loading, even at cyclic shear stresses lower than s_{u0} (Lefebvre and LeBoeuf 1987; Lefebvre and Pfendler 1996). Considering these compensating effects, Lefebvre and Pfendler (1996) suggested that the cyclic peak shear strength can be conservatively estimated as the peak strength obtained from monotonic tests at standard strain rates. In the present study, cyclic loading effects on shear strength degradation in the pre-peak zone are not modelled, which is assumed to be elastic. Moreover, the effect of strain-rate is not explicitly modelled. In other words, it is assumed that the peak s_u is not affected by the cyclic loading. Finally, the static shear stress in the soil elements near the slope could reduce the cyclic shear resistance (Lefebvre and Pfendler 1996), which has not been considered in this study.

The geotechnical parameters used for the “base case” analysis are listed in Table 1. The parameters are estimated from laboratory tests, interpretation of test data, constitutive model development and numerical studies on landslides in sensitive clays available in the literature (e.g.

Shannon and Wilson 1964; Mitchell et al. 1973; Woodward-Clyde 1982; Tavenas et al. 1983; Idriss 1985; Moriwaki et al. 1985; Stark and Contreras 1998; Bernander 2000; Leroueil 2001; Boulanger and Idriss 2004, Locat et al. 2008; Quinn 2009; Locat et al. 2011, 2013; Quinn et al. 2011).

A linearly increasing s_{u0} (kPa) = 25+2z is used for the sensitive clay layer, where z (in metres) is the depth below the upslope ground surface. It is assumed that geological effects, such as removal of soil in the downslope region that created the slope, has not changed the original undrained strength profile. As the ground surface is inclined in Slope-II (Fig. 1(b)), z is measured from the crest, while s_{u0} above the level of crest is assumed to be constant (= 25 kPa). The variation of s_u with depth (initial condition) and accumulated plastic shear strain (during failure) is implemented in Abaqus using the user-defined subroutine VUSDFLD. During the failure of a slope, a soil element might displace to different locations from its initial depth. In the subroutine, a code is written to ensure that the displaced soil elements carry the initial value of s_{u0}. The yield strength (= 2s_u, for the von Mises yield criterion) is given as a function of equivalent plastic shear strain ϵ_q^p (= PEEQVAVG in Abaqus), which is related to engineering plastic shear strain (γ^p) as $\epsilon_q^p = \gamma^p/\sqrt{3}$, where $\gamma^p = \delta/t_{FE}$ for simple shear condition and t_{FE} is the length of the cubical elements used in this study. The critical values of equivalent plastic shear strain required to define the stress–strain curve for FE input are shown above the horizontal axis in Fig. 3, where the superscript "p" represents the plastic shear strain.

Material Damping

The energy dissipation primarily occurs due to frequency-independent hysteretic behaviour of soil, which can be incorporated in dynamic FE analysis using a nonlinear stress–strain relationship (Kwok et al. 2007; Mánica et al. 2014; Tsai et al. 2014). As an elasto-plastic soil model is used in the present study, the plastic flow can simulate hysteretic damping when loading/unloading occurs from yield strength and therefore additional damping is required only in the elastic part (Zhai et al. 2004; Mánica et al. 2014). For cyclic loading inside the yield surface, energy dissipation can be achieved by nonlinear variation of stiffness with Masing's rule (Masing 1926; Chen and Qiu 2014) and viscous damping. As the main interest of the present study is to investigate large deformation failure of sensitive clay slopes, pre-yield stiffness variation is not considered, which requires an additional reliable soil model and is left for a future study. Mánica et al. (2014) compared the damping models available in FLAC (Itasca 2012) and the best performance was shown with the Rayleigh damping method for their problems. Similar to previous dynamic FE modelling using Abaqus, the material damping is incorporated using the Rayleigh damping (Martino and Mugnozza 2005; Ju and Ni 2007; Alipour and Zareian 2008; Jehel et al. 2014; Lindberg and Sandvik 2015). The stiffness proportional damping of $\beta = 0.000375$ is used. In Abaqus, the mass proportional damping is neglected in Eulerian materials.

FE Results

The development of failure planes with computational time, which is same as the time used for the earthquake input, is explained using the formation of shear bands due to strain-softening. Note, however, that the behaviour of soil is time-independent. For the soil parameters listed in Table 1 and $t_{FE} = 0.25$ m, s_u degradation initiates after $\epsilon_q^p = 0.014$ $(= \delta_{pc}/(\sqrt{3}t_{FE}))$ (e.g. point b in Fig. 3), and s_u reduces almost to s_{uR} at $\epsilon_q^p = 0.16$ $(= 2\delta_{95}/(\sqrt{3}t_{FE}))$ (e.g. point d in Fig. 3). As the failed soil blocks displace a large distance, the zones of very high ϵ_q^p represent the failure surfaces.

Slope-I

Figure 4 shows the progressive development of failure surfaces during the earthquake and post-quake stages for Slope-I (Fig. 1(a)). Global failure initiates with a rotational slide at $t = 8.5$ s of the earthquake (Fig. 4(a)). Rotational failure of another soil block, at a shallower depth than the previous one, occurs at $t = 12.25$ s (Fig. 4(b)). During this period ($t = 8.5$–12.25 s), the previously failed soil mass displaces a large distance in the downslope direction and is broken into smaller pieces by the formation of additional shear bands in it. The retrogressive failure of additional soil blocks and the displacement of failed soil mass continue with the earthquake although the amplitude of acceleration decreases with time after t~10 s (Figs. 4(c and d)). This is mainly due to the following reasons: (i) sufficiently large displacement of the failed soil mass reduces the support on the soil in the right side of the backscarp, (ii) relatively small earthquake acceleration after t~10 s is sufficient to cause failure of the soil behind the steep backscarp and (iii) kinematics of the failed soil mass is influenced by its displacement with time because of the reduction of s_u along the failure planes. Figures 4(f)–4(g) show the post-quake response of the slope. Although the earthquake stops at t~18.1 s, the failure process continues because of the reasons mentioned above. The lateral extent of the landslide (L_E) is the sum of "retrogression distance (L_R)", "slope length L_S", and "runout distance (L_U)" (Fig. 4(g)). In this study, L_R measures the horizontal distance from the crest of the slope to the furthest location of the shear band, which might be at the upslope ground surface on a global failure plane (e.g. point X in Fig. 4(g)) or at the tip of a local shear band (e.g. point Y in Fig. 11(l)). As will be discussed later, in some cases, the movement of failed soil (e.g. runout) is observed even at the end of the analysis period, especially when the downslope profile is inclined and $s_{u(ld)}$ is very small. Therefore, the maximum retrogression (L_{Rmax}) and runout (L_{Umax}) distances for these cases could not be obtained. In the following figures, for the purpose of comparison, the values of L_U and L_R at t = 30 s are reported as shown in Fig. 4(g), unless otherwise mentioned.

The rotational failure of successive soil blocks presented in Fig. 4 is similar to typical flowslides in sensitive clays—for example, the Notre-Dame-de-la-Salette slide in Quebec that was triggered by the 2010 Val de Bois earthquake (Perret et al. 2013; Demers et al. 2014). In that landslide, failure initiated near the toe of the slope and progressed in the upslope area in a stepped pattern—shallower depth of the bottom of the failure plane with the progress of retrogression—which is similar to the failure pattern shown in Fig. 4. Demers et al. (2014) reported that this type of stepped pattern of failure is commonly observed in sensitive clay slopes. Lefebvre et al. (1992) showed that, in the Sainte-Thècle failure triggered by the 1988 Saguenay earthquake, the base of the failure planes was approximately horizontal during upslope propagation of ~50 m and then failed along an inclined upward plane at the interface between the sensitive clay and till.

Effect of mesh size

FE analysis for the strain-softening material is challenging because the solution could be mesh size dependent. Various approaches have been used to reduce mesh dependency, as discussed in previous studies (e.g., Summersgill et al. 2017). During the post-peak softening stage, the strain is localized in the shear band. For sand, the thickness of the shear band (t_s) could be related to mean particle size (e.g., Guo 2012). For sensitive clays, the shear band thickness is generally small and its formation is complex, as reported from digital image analyses in laboratory tests (Thakur et al. 2018). Similarly, the characterization of shear bands based on field measurements is difficult. For example, Lehtonen et al. (2015) reported inconclusive locations of slip surface in a full-scale test of an embankment on sensitive clay, although they found a localized plastic shear deformation zone. The numerical simulation of such small thickness shear bands is not practical, and therefore, a computationally acceptable FE model can be developed using the element size scaling rule (Pietruszczak and Mróz 1981; Andresen and Jostad 2004; Soga et al. 2016). The thickness of finite element (t_{FE}) can be significantly larger than the real shear band thickness because the strain localization primarily occurs through one row of elements along the shear band (Anastasopoulos et al. 2007; Dey et al. 2015; Zhang et al. 2015). Therefore, in those studies, the simulations were performed adopting a scaling rule—the post-peak plastic shear strain required to mobilize a shear strength is inversely proportional to the thickness of the finite element. Some studies used a nonlocal regularization approach by spreading the localized strain over a predefined surrounding zone (D'Ignazio et al. 2017; Summersgill et al. 2017).

The importance of mesh-size regularization is shown by conducting analyses of Slope-I for three mesh sizes. As shown in Fig. 3 and Table 1, the post-peak plastic shear displacement, which is independent of mesh size, is used to define post-peak softening. However, for the input in FE modelling, the post-peak plastic shear strain (γ^p) is required, which is calculated as δ/t_{FE}, assuming the simple shear condition and $t_s = t_{FE}$. This implies that a faster s_u degradation behaviour should be used for a larger element. For example, s_{u95} mobilizes at $\gamma^p_{95} = \delta_{95}/t_{FE}$ of 3.5%, 7% and 14% for element sizes of 1.0 m, 0.5 m and 0.25 m, respectively, for the same δ_{95} = 0.035 m. Further discussion on this type of mesh regularization could be found in Dey et al. (2015) and Zhang et al. (2015). The analysis becomes computationally very expensive for a very small finite element size comparable to the shear zone thickness that observed in some post-slide investigations (few centimeters to few decimeters (Leroueil 2001)).

Figures 5(a, d and g) show that the formation of the shear bands at t = 8.5 s is very similar for all three mesh sizes. For t = 17 s and 30 s, the extent of the failure zone is very comparable; however, diffused plastic zones form in the coarse mesh model and the failure pattern is not clear (e.g. Figs. 5(h and i)) while the shear bands are clear in the fine mesh model (e.g., Figs. 5(b and c)).

Simulation is also performed with 0.5 m mesh but without mesh regularization (Fig. 5(j–l)). Comparison between Figs. 5(d–f) and 5(j–l) shows that the extent of failure is significantly smaller when mesh regularization is not considered. Debnath et al. (2018) conducted large deformation FE simulations of rapid offshore slope failure and run-out using the numerical approach presented in this study and compared the results with computational fluid dynamics simulations and showed that the mesh convergence can be achieved simply by reducing the mesh size if the soil does not have strain-softening behaviour. The present study shows that, in addition to small mesh size, an element size scaling rule is required for strain-softening materials.

In the present study, except for Figs. 5 (d–l) (e.g. mesh sensitivity), all the analyses are performed with 0.25 m cubical elements.

Effect of slope angle

Figure 6 shows the results for three slope angles with a constant slope height (15 m). Global failure occurs quickly in the steep slope during the earthquake (Fig. 6(a)); however, at this time (t = 8.5 s) no plastic shear strain generates in the gentle slope (Fig. 6(g)). Retrogressive failure of a number of soil blocks occurs during and after seismic acceleration. Both L_R and L_U increase with an increase in steepness of the slope (Fig. 6(c, f and i)). Locat et al. (2013) showed the increase of retrogression with slope angle, except for a high coefficient of earth pressure at rest, for the failure triggered by toe erosion.

Maximum retrogression and runout distances

Based on post-slide investigations, attempts have been made in the past to relate flowslide potential with topography (e.g. slope geometry, downslope gradient), geotechnical properties (e.g.

remoulded shear strength, sensitivity, liquidity index and stability number) and percentage of sensitive clay volume in the sliding mass (Tavenas 1984; Leroueil et al. 1996; Strand et al. 2017). Thakur and Degago (2014) proposed a simplified analytical method for estimation of flowslide potential based on remoulding energy (Tavenas et al. 1983). Simplified methods have been proposed to estimate the maximum retrogression distance (Mitchell and Markell 1974; Carson 1979; Quinn et al. 2011); however, Demers et al. (2014) found a large discrepancy in estimated values using these methods when compared with historical landslide data in Québec, Canada. The effects of downslope profile and strain-softening behaviour are examined with 12 simulations with soil parameters listed in Table 1, unless otherwise mentioned.

Two simulations are performed with a downslope profile (ba in Fig. 1(a)) inclined downward at 3° and 5° to the horizontal, while the main slope (bc) is same as the one above (2:1). The maximum runout distance for 3° is higher (169 m) than that calculated for a flat downslope profile (0°) (120 m) (Case III in Table 2); however, the maximum retrogression distance is almost the same (~ 61 m) in both cases. For a 5° inclined downslope, the runout did not stop because the remoulded soil can flow on this inclined surface as $s_{u(ld)}$ is very small. Note that, in the field, runout might be stopped when the movement of the failed soil is obstructed by the other bank of the river, as happened in the 2010 Saint-Jude landslide in Quebec (Locat et al. 2017).

In order to investigate the effect of post-peak softening behaviour, a total of 10 simulation results for varying s_{uR}, $s_{u(ld)}$, δ_{95} and δ_{ld} is summarized in Table 2. For brevity, instead of presenting progressive failure with time, as shown in Figs. 4–6, the maximum retrogression (L_{Rmax}) and runout (L_{Umax}) distances, together with retrogression in the upslope areas, are shown in Table 2. The slip surfaces shown in the figures in the last column of Table 2 are drawn through the highly concentrated plastic shear strain zones when the failure of a soil block occurs from the intact soil. The following are the key observations from these simulations.

i) The failure of a new soil block, not only the first one but also in retrogression, initiates with a rotational slide, except for the detachment of some soil blocks in Cases-VII and VIII (triangular blocks M1–M5). However, during downslope movement, the failed soil blocks breaks into smaller pieces due to the formation of shear bands at an approximately 45° angle to the horizontal. Therefore, for a large displacement, some of the soil blocks look like horsts, as is commonly observed in spread type failure (Fig. 4(g)). The depth of rotational slides decreases with retrogression for the cases with a low s_{u0}/s_{uR} (e.g. Cases-I–VI). Note that a decrease in depth of the sliding plane has been observed in the field for some landslides, as discussed above. The width of the zone of plastic shear strain around the failure planes increases with displacement (e.g. Fig. 4(g)), which causes remoulding of the soil and thereby runout potential.

ii) Comparison of the simulation results for cases III, IX and X shows that a decrease in δ_{95} increases the maximum retrogression and runout distances, which is because of the increase in the general brittleness index of the soil (= $(s_{u0} - s_u)/s_{u0}$) (D'Elia et al. 1998). This trend is similar to sensitive clay slope failure due to toe erosion (Locat et al. 2013; Dey et al. 2015).

iii) For a given s_{u0}, the reduction of s_{uR} also increases the general brittleness index. With an increase in s_{u0}/s_{uR} ratio, the maximum retrogression and runout distances increase (compare Cases III, VII and VIII). Moreover, the failure pattern changes from flowslide to a combination of flowslide and spread with an increase in s_{u0}/s_{uR} ratio (Cases III and VII). The Λ- and V-shaped blocks are similar to horsts and grabens, respectively, which are commonly observed in the spread. Similar composite failure patterns—rotational flowslide followed by a spread with the formation of horsts and grabens—have been reported for the Mink Creek landslides in British Columbia, Canada (Geertsema et al. 2006). The tip angle of the horst is 90° because the simulation is performed for $\phi = 0$ condition. However, in the spreads in eastern Canada, the horst tip angle of 50°–70° has been observed (Locat et al. 2011). More advanced soil model might be able to simulate this shape of the horst.

iv) Both retrogression and runout distances increase when post-peak reduction of s_u occurs quickly. Strain-softening immediately after the peak (bcd in Fig. 3) influences primarily the retrogression (compare Cases III, VII and VIII), while the second part (de in Fig. 3) has more influence on runout than retrogression (compare Cases I–V). For the cases listed in Table 2, L_{Umax}/L_{Rmax} = 0.9–3.4. Note that based on field observations, Thakur (2016) showed L_{Umax}/L_{Rmax}~0.5–3.0 for a varying downslope terrain and failure type.

v) An increase in mobility of debris—due to low shear strength at large strains and/or increase in downslope gradient—increases flowslide potential. This is similar to previous studies, where it is shown that a low residual shear strength and favourable downslope topography increase flowslide potential together with an increase in runout and retrogression distances (Mitchell and Markell 1974; Thakur 2016).

vi) Figure 7(a) shows that both retrogression and runout distances decrease with an increase in remoulded energy (E_R). Here E_R is calculated as the area below the stress–strain curve up to point e in Fig. 3 (Tavenas et al. 1983; Thakur and Degago 2014). In the present study, s_{u0} in the sensitive clay layer increases with depth; therefore, E_R is calculated based on the average peak shear strength between the ground surface and toe level (= 40 kPa). Moreover, the trend line for retrogression in Fig. 7(a) is drawn without Cases-VII and VIII because in these cases the failure involves both flowslide and spread. Figure 7(b) shows that L_{Umax} and L_{Rmax} increase with kinetic energy (E_k). Here, E_k is calculated by subtracting E_R from potential energy (=

$2\gamma H/3$, where H is the height of the slope) (Thakur and Degago 2014). Finally, although the data points are scattered, Fig. 7(c) shows a trend: the higher the retrogression distance, the higher the runout distance. Similar trends for L_{Umax} and L_{Rmax} have been reported from field observations (Tavenas et al. 1983; Thakur and Degago 2014).

Slope-II: Slightly inclined upslope ground surface

Figure 8 shows the dynamic FE simulation results for Slope-II (Fig. 1b) with an upslope ground surface inclination $\alpha = 3°$. To ensure that the slope is stable under gravity load, the height of the slope considered in this case is 10 m (cf. 15 m in Slope-I, III and IV). During the initial stage of the earthquake, a horizontal shear band develops (Fig. 8(a)). With the continuation of earthquake loading, the soil mass above the horizontal shear band breaks into V- and Λ-shaped blocks forming horsts and grabens (Figs. 8(b–d)). The propagation of the horizontal shear band continues during the last stage of the earthquake (t = 17–19.95s) and post-quake stage because of displacement of the failed soil mass. At t = 25 s, a large monolithic slab fails causing huge retrogression, L_{R} = 159.2 m (Fig. 8(e)). The failed soil blocks displace further, which creates a large graben near the backscarp by the formation of another inclined shear band (Fig. 8(f)). Dislocation of large monolithic slabs was observed along B-Street and D-Street after the Alaska earthquake (Moriwaki et al. 1985), which occurred due to undrained shear strength loss of the sensitive Bootlegger Cove clay (Stark and Contreras 1998). Monolithic slab type failure of sensitive clay slopes has also been reported in other studies (Legget and LaSalle 1978; Desjardins 1980; Karlsrud et al. 1985). The present FE analysis can explain some of the mechanisms that could cause this type of failure.

The effects of α on failure mechanism are shown in Fig. 9. For small α (= 1.5°), rotational failure of only one soil block occurs. For $\alpha = 3°$, in addition to rotational slides near the toe, a large monolithic slide occurs, as discussed in previous sections. However, for $\alpha = 4°$, only two rotational slides occur without any monolithic slide. Very small retrogression occurs for $\alpha = 4°$ ($L_R = 65.2$ m) compared to the analysis for $\alpha = 3°$ ($L_R = 159.2$ m) (Figs. 9 (f and i)). These simulations show that a favourable α is required for a monolithic slide, and for the conditions used here, it occurs at $\alpha = 3°$.

Slope-III: With an upslope distributed load

Upslope loading might significantly affect the failure of slopes, which has been observed in the field and verified with numerical modeling for monotonic loading (Bernander 2000; Bernander et al. 2016; Wang et al. 2013; Dey et al. 2016a; Wang and Hawlader 2017) and dynamic loading (Seed and Wilson, 1967; Barnhardt et al. 2000; Kourkoulis et al. 2010). Figure 10 shows the formation of failure planes when a uniform surcharge q = 80 kPa exists at 100 m distance from the crest. The slope is stable and there is no plastic shear strain below the surcharge at the end of the gravity step. With dynamic loading, rotational failure occurs by formation of a number of global failure planes (Figs. 10(a–d)). At the same time, a steep shear band generates below the surcharge (Fig. 10(c)). As the movement of the failed soil mass continues, additional shear bands form, causing retrogressive failure of the slope during the earthquake and post-quake stages (Figs. 10(e and f)). The number of shear bands below the surcharge increases and finally a long horizontal shear band joins the two failure zones. A similar type of large graben formation below the loaded areas has been inferred from post-slide investigations of the L-Street slide due to the 1964 Alaskan earthquake (Moriwaki et al. 1985). Note however that, in the field, the shear strength of soil under the loaded area might be changed due to consolidation, which has not been considered in the present FE simulations.

A parametric study is conducted varying q between 0 and 80 kPa (Fig. 11). The extent and pattern of failure for $q = 0$ and 20 kPa are similar (Figs 11(a–f)). The influence of q on slope failure is found for $q = 40$ kPa, which increases L_R by 8.5 m compared to the no-surcharge case (Figs. 11(c and i)). For a large q (= 80 kPa), slope failure planes join the failure planes below the surcharge through the formation of an additional horizontal shear band. Note that the distance of the surcharge load from the crest also influences the failure of the slope (Dey et al. (2016a).

Slope-IV: Highly sensitive clay at toe depth

The existence of a thin weak layer has been considered as a potential reason for many large-scale landslides. After the 1964 Alaskan earthquake, tests were conducted building model slopes with a thin extremely weak soil layer at the depth of the toe to understand retrogressive failure mechanisms. Figure 12 shows the effects of a highly sensitive clay layer ($s_{u0}/s_{uR} = 30$) of thickness $H_q = 3.0$ m on slope failure. The first shear band does not form horizontally through the highly sensitive clay layer; instead, a curved failure plane forms along the critical location (Fig. 12(a)). After that, a shear band propagates almost horizontally through the highly sensitive clay layer (Figs. 12(b-f)). Because of the highly sensitive clay layer, the failure surfaces develop very quickly compared to Slope-I (cf. Fig. 4). The horizontal shear band through the highly sensitive clay layer develops rapidly and the failed soil blocks dislocate very quickly in the downslope direction, resulting in formation of a number of horsts and grabens (Figs. 12(e–f)). Similar failures have been observed in the field. For example, the Turnagain Heights landslide triggered by the 1964 Alaskan earthquake shows a similar failure pattern (Seed and Wilson 1967; Barnhardt et al. 2000).

Figure 13 shows a parametric study for the thickness of the highly sensitive clay layer, H_q (= 1.0–6.0 m). The bottom of the highly sensitive clay layer is placed at the level of the toe of the slope. As the height of the slope is the same (15 m), the thickness of the overlain sensitive clay layer varies between 9.0 and 14 m. At t = 8.5 s, the rotational slide of the first soil block is very similar for all three cases (Figs. 13(a, d and g)). The retrogression process is slow for H_q = 6.0 m (Fig. 13(h)) compared to the other two cases (Figs. 13(b and e), because the failure planes tend to propagate upward in the cases of a thick highly sensitive clay layer. For H_q = 6.0 m, after the first rotational slide, shallow retrogressive failure occurs. However, for a thin H_q, a horizontal shear band forms first and then the inclined shear bands generate in the overlain sensitive clay with displacement of the failed soil blocks (Figs. 13(b and e)). At t = 30 s, the maximum retrogression (L_R = 180 m) is found for the thinnest case (Fig. 13 (c)). Slightly more runout is found for H_q = 6.0 m because a large volume of extremely weak highly sensitive clay facilitates downslope sliding of the failed soil blocks (Fig. 13 (h and i)).

Conclusions

Post-slide investigations show that many large-scale landslides in sensitive clays due to earthquake involve the failure of a number of soil blocks commonly classified as spread, flowslide and/or monolithic slides. These types of landslide cannot be analyzed using the traditional limit equilibrium or Lagrangian-based FE methods because the failure surfaces develop progressively and extremely large strains generate along the failure planes that causes numerical instability in typical Lagrangian FE analysis. This paper presents large deformation FE modelling of the failure of sensitive clay slopes due to an earthquake. Dynamic FE simulations are performed for four hypothetical slope profiles for a given earthquake acceleration–time history. The failure initiates with a rotational slide of a soil block and then retrogresses in the upslope areas during the earthquake and also in the post-quake phase. FE simulations show that significant retrogression and runout could occur in the post-quake phase, which is similar to many post-slide field observations.

The following conclusions are drawn from this study:

a) The geometry of the slope and soil properties significantly influence failure patterns. The faster the reduction of shear strength after the peak (increased general brittleness index), the larger the extent of failure. Low shear strength at large strains and increasing downslope gradient increase the mobility of the failed soil mass and thereby landslide extent, especially runout.

b) An increase in remoulding energy reduces the retrogression and runout distances. For Slope-I, the ratio between the maximum runout and retrogression distance is 0.9–3.4.

c) A large monolithic slide might occur for a favourable upslope ground surface inclination. However, a lesser extent of failure is found for higher or lower upslope angles than for the favourable one.

d) For the cases analyzed, most of the failure of soil blocks from intact soil occurs by a rotational slide, except for Slope-IV. However, in some cases, after retrogression to a certain distance, the failure pattern changes to spread (horst and graben) and monolithic slide of a large block, which indicates that a combination of different types of failure is possible in a large landslide, as reported from post-slide investigations in some studies.

e) A sufficiently large upslope surcharge exacerbates slope failure. A deep-seated graben forms under the loaded area, as observed in the field (e.g. after the 1964 Alaskan earthquake).

f) A highly sensitive clay layer at the level of the toe increases the propagation propensity of the horizontal shear band which causes spread type failure (Slope-IV). The propagation is higher for a thin highly sensitive clay layer case as compared to a thick one.

Although the analysis presented in this study is for idealized slopes, the numerical modelling technique has profound engineering implications. The empirical correlations proposed in previous studies—as a function of different parameters such as stability number, remoulded shear strength, liquidity index, and soil sensitivity—can be used for an estimation of retrogression and runout distance. Recognizing the significant uncertainties in such estimation, site-specific numerical analyses can be performed for the critical sections of the slope, using the method presented in this study. However, for this type of large deformation FE analysis, a proper estimation of geotechnical parameters and earthquake acceleration–time history is required. Further research is warranted on modelling of soil, especially the strain-softening behaviour of sensitive clays under dynamic loading.

Acknowledgements

The works presented in this paper have been supported by the Natural Sciences and Engineering Research Council of Canada (NSERC), Mitacs, Research and Development Corporation of Newfoundland and Labrador (RDC NL), and Petroleum Research Newfoundland and Labrador (PRNL).

List of Symbols

The following symbols are used in this paper:

α upslope ground inclination

β stiffness proportional damping

δ_t accumulated shear displacement

δ_e elastic shear displacement

δ accumulated plastic shear displacement during strain softening

δ_{95}	δ at which s_u reduced by 95% of (s_{u0} - s_{uR})
δ_{pc}	accumulated plastic shear displacement for initiation of strain-softening
ϵ_q^p	equivalent plastic shear strain
γ^p	engineering plastic shear strain
n	exponent for K_0 for OC clay
ν_u	undrained Poisson's ratio
E_k	kinetic energy
E_R	remoulded energy
E_u	undrained Young's modulus
H_q	highly sensitive clay layer thickness (Slope-IV)
K_0	earth pressure coefficient at-rest
$K_{0(NC)}$	K_0 for NC clay
L_R	retrogression distance
L_S	slope length
L_U	runout distance
L_{Rmax}	maximum retrogression distance
L_{Umax}	maximum runout distance
M	magnitude of earthquake
OCR	overconsolidation ratio
q	upslope vertical surcharge
s_u	mobilized undrained shear strength
s_{u0}	initial peak undrained shear strength
s_{uR}	s_u mobilized in shear band at considerable shear displacement

$s_{u(ld)}$ s_u at very large displacements

t_{FE} length of cubical elements used in FE analysis

t_s thickness of shear band

z depth below the crest of the slope

References

Alipour, A., and Zareian, F. 2008. Study Rayleigh damping in structures; uncertainties and treatments. *In* Proceedings of 14th World Conference on Earthquake Engineering, Beijing, China, pp. 1-8.

Anastasopoulos, I., Gazetas, G., Bransby, M. F., Davies, M. C. R., and El Nahas, A. 2007. Fault rupture propagation through sand: finite-element analysis and validation through centrifuge experiments. Journal of Geotechnical and Geoenvironmental Engineering, **133**(8): 943–958.

Andresen, L., and Jostad, H. P. 2004. Analyses of progressive failure in long natural slopes. Numerical Models in Geomechanics: *In* Proceedings of the 9th International Symposium on Numerical Models in Geomechanics, NUMOG IX, Ottawa, Ontario, pp. 25–27.

Aylsworth, J. M., and Lawrence, D. E. 2003. Earthquake-induced landsliding east of Ottawa; a contribution to the Ottawa Valley Landslide Project. *In* Proceedings of the 3rd Canadian Conference on Geotechnique and Natural Hazards, Edmonton, Alberta, pp. 77–84.

Barnhardt, W. A., and Kayen, R. E. 2000. Radar structure of earthquake-induced, coastal landslides in Anchorage, Alaska. Environmental Geoscience, **7**(1): 38–45.

Benson, D. J. 1992. Computational methods in Lagrangian and Eulerian hydrocodes. Computer Methods in Applied Mechanics and Engineering, **99**(2): 235–394.

Benson, D. J., and Okazawa, S. 2004. Contact in a multi-material Eulerian finite element formulation. Computer Methods in Applied Mechanics and Engineering, **193**(39): 4277–4298.

Bernander, S. 2000. Progressive failure in long natural slopes: formation, potential extension and configuration of finished slides in strain-softening soils. Master's thesis, Luleå University of Technology, Luleå, Sweden.

Bernander, S., Kullingsjö, A., Gylland, A. S., Bengtsson, P. E., Knutsson, S., Pusch, R., Olofsson, J., and Elfgren, L. 2016. Downhill progressive landslides in long natural slopes: triggering agents and landslide phases modeled with a finite difference method. Canadian Geotechnical Journal, **53 (**10): 1565–1582.

Boulanger, R. W., and Idriss, I. M. 2004. Evaluating the potential for liquefaction or cyclic failure of silts and clays, Report UCD. CGM-04/01, Center for Geotechnical Modeling, University of California, Davis, CA.

Brooks, G. R. 2013. A massive sensitive clay landslide, Quyon Valley, southwestern Quebec, Canada, and evidence for a paleoearthquake triggering mechanism. Quaternary Research, **80 (**3): 425–434.

Carson, M. A. 1977. On the retrogression of landslides in sensitive muddy sediments. Canadian. Geotechnical Journal, **14**(4): 582–602.

Carson, M. A. 1979. Le glissement de Rigaud (Québec) du 3 Mai 1978 : une interprétation du mode de rupture d'après la morphologie de la cicatrice. Géographie physique et Quaternaire, **33**(1): 63–92.

Chen, W., and Qiu, T. 2014. Simulation of earthquake-induced slope deformation using SPH method. International Journal for Numerical and Analytical Methods in Geomechanics, **38**(3): 297–330.

Debnath, B., Hawlader, B., Dutta, S., and Sheel, T. 2018. Performance of computational fluid dynamics and finite element methods for modeling downslope displacement of failed soil from submarine landslides. Geohazards 7. June 3–6, 2018, Canmore, Alberta, Canada.

Demers, D., Robitaille, D., Locat, P., and Potvin, J. 2014. Inventory of large landslides in sensitive clay in the province of Quebec, Canada: preliminary analysis. *In* Landslides in Sensitive Clays: from Geosciences to Risk Management, Advances in Natural and Technological Hazards Research (L'Heureux, J. S., Locat, A., Leroueil, S., Demers, D. and Locat. J. (eds.)). Dordrecht, the Netherlands: Springer, **36**, pp. 77–89.

Desjardins, R. 1980. Tremblements de terre et glissements de terrain: Corrélation entre des datations au 14C et des données historiques à Shawinigan, Québec. Géographie physique et Quaternaire, **34**(3): 359–362.

Dey, R., Hawlader, B., Phillips, R., and Soga, K. 2015. Large deformation finite-element modeling of progressive failure leading to spread in sensitive clay slopes. Géotechnique, **65**(8): 657–668.

Dey, R., Hawlader, B., Phillips, R., and Soga, K. 2016a. Numerical modeling of combined effects of upward and downward propagation of shear bands on stability of slopes with sensitive clay. International Journal for Numerical and Analytical Methods in Geomechanics, **40**(15): 2076–2099.

Dey, R., Hawlader, B., Phillips, R., and Soga, K. 2016b. Modeling of large-deformation behaviour of marine sensitive clays and its application to submarine slope stability analysis. Canadian Geotechnical Journal, **53**(7): 1138–1155.

Dey, R., Hawlader, B., Phillips, R., and Soga, K. 2016c. Numerical modeling of submarine landslides with sensitive clay layers. Géotechnique, **66**(6): 454–468.

D'Elia, B., Picarelli, L., Leroueil, S., and Vaunat, J. 1998. Geotechnical characterisation of slope movements in structurally complex clay-soils and stiff jointed clays. Italian Geotechnical Journal, **32**(3): 5–32.

Díaz-Rodríguez, J. A., and López-Molina, J. A. 2008. Strain thresholds in soil dynamics. *In* Proceedings of the 14th World Conference on Earthquake Engineering, Beijing, China, **1**, pp. 12–17.

D'Ignazio, M., Länsivaara, T.T., and Jostad, H.P. 2017. Failure in anisotropic sensitive clays: finite element study of Perniö failure test. Can. Geotech. J. **54**: 1013–1033.

Duncan, J. M. 1996. State of the art: limit equilibrium and finite-element analysis of slopes. Journal of Geotechnical Engineering, **122**(7): 577–596.

Dutta, S., Hawlader, B., and Phillips, R. 2015. Finite element modeling of partially embedded pipelines in clay seabed using Coupled Eulerian–Lagrangian method. Canadian. Geotechnical Journal, **52**(1): 58–72.

Einav, I., and Randolph, M. F. 2005. Combining upper bound and strain path methods for evaluating penetration resistance. International. Journal for Numerical Methods in Engineering, **63**(14): 1991–2016.

Geertsema, M., Cruden, D. M., and Schwab, J. W. 2006. A large rapid landslide in sensitive glaciomarine sediments at Mink Creek, northwestern British Columbia, Canada. Engineering Geology, **83**: 36–63.

Griffiths, D. V., and Lane, P. A. 1999. Slope stability analysis by finite elements. Géotechnique, **49**(3): 387–403.

Guo, P. 2012. Critical length of force chains and shear band thickness in dense granular materials. Acta Geotech., **7**: 41–55.

Gylland, A. S., Rueslåtten, H., Jostad, H. P., and Nordal, S. 2013. Microstructural observations of shear zones in sensitive clay. Engineering Geology, **163**: 75–88.

Hamouche, K.K., Leroueil, S., Roy, M., and Lutenegger, A.J. 1995. In situ evaluation of K_0 in eastern Canada clays. Canadian Geotechnical Journal, **32(**4): 677–688.

Idriss, I. M. 1985. Evaluating seismic risk in engineering practice. *In* Proceedings of the 11th International Conference on Soil Mechanics and Foundation Engineering, San Francisco, pp. 255–320.

Idriss, I. M., and Sun, J. I. 1991. Users' manual for SHAKE91: a modified version of SHAKE for conducting equivalent linear seismic response analyses of horizontally layered soil deposits. Centre for Geotechnical Modelling, University of California, Berkeley, California, USA.

Islam, N. 2017. Numerical implementation and modeling of earthquake induced landslides for slopes with soft and sensitive clay layers. Master's Thesis, Memorial University of Newfoundland, Canada.

Islam, N., Hawlader, B., Wang, C., and Soga, K. 2017. Implementation of a large deformation finite element modeling technique for seismic slope stability analyses. Soil Dynamics and Earthquake Engineering (under review).

Itasca 2012. FLAC3D. Fast lagrangian analysis of continua in 3-dimensions, version 5.0, manual. Itasca, Minnesota.

Javed, K. 2011. Behavior of sensitive clay subjected to static and cyclic loading, PhD thesis, Concordia University, Montreal, Quebec, Canada.

Jehel, P., Léger, P., and Ibrahimbegovic, A. 2014. Initial versus tangent stiffness-based Rayleigh damping in inelastic time history seismic analyses. Earthquake Engineering and Structural Dynamics, **43**(3):467–484.

Ju, S. H., and Ni, S. H. 2007. Determining Rayleigh damping parameters of soils for finite element analysis. International Journal for Numerical and Analytical Methods in Geomechanics, **31(**10): 1239–1255.

Kakoli, S. T. N. 2005. Behaviour of sensitive clay under cyclic loading, Master's Thesis, Concordia University, Montreal, Quebec, Canada.

Karlsrud, K., Aas, G., and Gregersen, O. 1985. Can we predict landslide hazards in soft sensitive clays? Summary of Norwegian practice and experiences. NGI Publication, **158**.

Keefer, D. K. 1984. Landslides caused by earthquakes. Geological Society of America Bulletin, **95**(4): 406–421.

Kourkoulis, R., Anastasopoulos, I., Gelagoti, F., and Gazetas, G. 2010. Interaction of foundation−structure systems with seismically precarious slopes: Numerical analysis with strain softening constitutive model. Soil Dynamics and Earthquake Engineering, **30(**12): 1430–1445.

Kramer, S. L. 1996. Geotechnical earthquake engineering. Upper Saddle River, N.J.: Prentice Hall.

Kwok, A. O., Stewart, J. P., Hashash, Y. M. A., Matasovic, N., Pyke, R., Wang, Z., and Yang, Z. 2007. Use of exact solutions of wave propagation problems to guide implementation of nonlinear seismic ground response analysis procedures. Journal of Geotechnical and Geoenvironmental Engineering, **133**(11): 1385–1398.

Lefebvre, G., Bozozuk, M., Philibert, A., and Hornych, P. 1991. Evaluating K_0 in Champlain clays with hydraulic fracture tests. Canadian Geotechnical Journal, **28**(3): 365–377.

Lefebvre, G., and LeBoeuf, D. 1987. Rate effects and cyclic loading of sensitive clays. Journal of Geotechnical Engineering, **113**(5): 476–489.

Lefebvre, G., Leboeuf, D., Hornych, P., and Tanguay, L. 1992. Slope failures associated with the 1988 Saguenay earthquake, Quebec, Canada. Canadian Geotechnical Journal, **29**(1): 117–130.

Lefebvre, G., and Pfendler, P. 1996. Strain rate and preshear effects in cyclic resistance of soft clay. Journal of Geotechnical Engineering, **122**(1): 21–26.

Legget, R. F., and LaSalle, P. 1978. Soil studies at Shipshaw, Quebec: 1941 and 1969. Canadian Geotechnical Journal, **15(**4): 556–564.

Lehtonen, V., Meehan, C., Länsivaara, T., and Mansikkamäki, J. 2015. Full-scale embankment failure test under simulated train loading. Géotechnique **65**(12): 961–974.

Leroueil, S. 2001. Natural slopes and cuts: movement and failure mechanisms. Géotechnique, **51**(3): 197–243.

Leroueil, S., Vaunat, J., Picarelli, L., Locat, J., Faure, R., and Lee, H. 1996. A geotechnical characterization of slope movements. *In* Proceedings of the 7th International Symposium on Landslides, Senneset K. (ed) Trondheim. Balkema, Rotterdam, pp. 53–74.

Lindberg, S., and Sandvik, P. 2015. A comparison of finite element formulations for analysis of the converting process of packaging materials. Master's Thesis, Chalmers University of Technology, Göteborg, Sweden.

Lo, K. Y., and Lee, C. F. 1973. Stress analysis and slope stability in strain-softening materials. Géotechnique, **23(**1): 1–11.

Locat, A., Leroueil, S., Bernander, S., Demers, D., Locat, J., and Ouehb, L. 2008. Study of a lateral spread failure in an eastern Canada clay deposit in relation with progressive failure: the Saint-Barnabé-Nord slide. *In* Proceedings of the 4th Canadian conference on geohazards: from causes to management, Québec, Canada, pp. 89–96.

Locat, A., Leroueil, S., Bernander, S., Demers, D., Jostad, H. P., and Ouehb, L. 2011. Progressive failures in eastern Canadian and Scandinavian sensitive clays. Canadian Geotechnical Journal, **48(**11): 1696–1712.

Locat, A., Jostad, H. P., and Leroueil, S. 2013. Numerical modeling of progressive failure and its implications for spreads in sensitive clays. Canadian Geotechnical Journal, **50**(9): 961–978.

Locat, A., Locat, P., Demers, D., Leroueil, S., Robitaille, D., and Lefebvre, G. 2017. The Saint-Jude landslide of 10 May 2010, Quebec, Canada: Investigation and characterization of the landslide and its failure mechanism. Canadian Geotechnical Journal, **54**(10): 1357-1374.

Mánica, M., Ovando, E., and Botero, E. 2014. Assessment of damping models in FLAC. Computers and Geotechnics, **59:** 12–20.

Martino, S., and Mugnozza, G. S. 2005. The role of the seismic trigger in the Calitri landslide (Italy): historical reconstruction and dynamic analysis. Soil Dynamics and Earthquake Engineering, **25**(12): 933–950.

Masing, G. 1926. Eigenspannungen und verfertigung beim messing (Fundamental stresses and strengthening with brass). *In* Proceeding of the 2nd International Congress on Applied Mechanics, Zurich, pp. 332–335.

Mitchell, J. K., Houston, W. N., and Yamane, G. 1973. Sensitivity and geotechnical properties of bootlegger cove clay, The Great Alaska Earthquake of 1964, Committee on the Alaska Earthquake of the division of earth sciences, National Research Council, pp. 1-104.

Mitchell, R. J., and Markell, A. R. 1974. Flowsliding in sensitive soils. Canadian Geotechnical Journal, **11**(1): 11–31.

Moriwaki, Y., Vicente, E. E., Lai, S., and Moses, T. L. 1985. A re-evaluation of the 1964 “L” Street Slide. State of Alaska, Department of Transportation and Public Facilities, pp. 1-135.

Nadim, F. 1998. Slope stability under earthquake loading. Appendix F in Seabead project. NGI Report 982512-2.

Odenstad, S. 1951. The landslide at Sköttorp on the Lidan River, February 2, 1946. *In* Proceedings of the Royal Swedish Geotechnical Institute, **4**, pp. 5–39.

Palmer, A. C., and Rice, J. R. 1973. The growth of slip surfaces in the progressive failure of over-consolidated clay. Proceedings of the Royal Society, London, **332**(1591): 527–548.

Park, D. S., and Kutter, B. L. 2015. Static and seismic stability of sensitive clay slopes. Soil Dynamics and Earthquake Engineering, **79**: 118–129.

PEER (Pacific Earthquake Engineering Research Center) 2010. Ground motion database. See http://peer.berkeley.edu/smcat/

Perret, D., Mompin, R., Demers, D., Lefebvre, G., and Pugin, A. J. M. 2013. Two large sensitive clay landslides triggered by the 2010 Val-Des-Bois Earthquake, Quebec (Canada) Implications for Risk Management. *In* Proceedings of the 1st International Workshop on Landslides in Sensitive Clays (IWLSC), Quebec City, Quebec.

Pestana, J. M., and Nadim, F. 2000. Nonlinear site response analysis of submerged slopes. Report No. UCB/GT/2000-04. The University of California, Berkeley, USA, 51p.

Pietruszczak, S. T., and Mróz, Z. 1981. Finite element analysis of deformation of strain-softening materials. International. Journal for Numerical Methods in Engineering, **17**(3): 327–334.

Qiu, G., Henke, S., and Grabe, J. 2011. Application of a Coupled Eulerian–Lagrangian approach on geomechanical problems involving large deformations. Computers and Geotechnics, **38**(1): 30–39.

Quinn, P. 2009. Large landslides in sensitive clay in eastern Canada and the associated hazard and risk to linear infrastructure. Ph.D. Thesis, Queen's University, Kingston, Ontario, Canada.

Quinn, P. E., Diederichs, M. S., Rowe, R. K., and Hutchinson, D. J. 2011. A new model for large landslides in sensitive clay using a fracture mechanics approach. Canadian Geotechnical Journal, **48**(8): 1151–1162.

Quinn, P. E., Diederichs, M. S., Rowe, R. K., and Hutchinson, D. J. 2012. Development of progressive failure in sensitive clay slopes. Canadian Geotechnical Journal, **49**(7): 782–795.

Quinn, P. E., and Zaleski, M. 2015. Co-seismic large landslides in sensitive clay in eastern Canada, a search for an initiation threshold. *In* Proceedings of the 68th Canadian Geotechnical Conference, Québec City, Québec.

Rasmussen, K. K. 2012. An investigation of monotonic and cyclic behaviour of Leda clay, Ph.D. thesis, The University of Western Ontario, Canada.

Seed, H. B., and Wilson, S. D. 1967. The Turnagain heights landslide in Anchorage, Alaska. Journal of Soil Mechanics and Foundations Division, ASCE, **93**(4): 325–353.

Seed, H. B. 1979. Considerations in the earthquake-resistant design of earth and rockfill dams. Géotechnique, **29**(3): 215–263.

Shannon, and Wilson 1964. Report on Anchorage area soil studies, Alaska, to U.S. Army Engineer District, Anchorage, Alaska.

Soga, K., Alonso, E., Yerro, A., Kumar, K., and Bandara, S. 2016. Trends in large-deformation analysis of landslide mass movements with particular emphasis on the material point method. Géotechnique, **66** (3): 248–273.

Stark, T. D., and Contreras, I. A. 1998. Fourth Avenue landslide during 1964 Alaskan earthquake. Journal of Geotechnical and Geoenvironmental Engineering, **124**(2): 99–109.

Strand, S., Thakur, V., L'Heureux, J., Lacasse, S., Karlsrud, K., Nyheim, T., Aunaas, K., Ottesen, H., Gjelsvik, V., Fauskerud, O., Sandven, R., and Åkershult, A. 2017. Runout of landslides in sensitive clays. Landslides in Sensitive Clays, From Research to Implementation, Vikas - Thakur, Jean-Sébastien L'Heureux and Ariane Locat eds., pp. 289–300.

Summersgill, F.C., Kontoe, S., and Potts, D.M. 2017. On the use of nonlocal regularisation in slope stability problems. Computers and Geotechnics, **82**:187–200.

Tavenas, F. 1984. Landslides in Canadian sensitive clays – a state of the art. *In* Proceedings of the 4th International Symposium on Landslides. Canadian Geotechnical Society, **1**, pp.141–153.

Tavenas, F., Flon, P., Leroueil, S., and Lebuis, J. 1983. Remolding energy and risk of slide retrogression in sensitive clays. *In* Proceedings of the Symposium on Slopes on Soft Clays, Linköping, Sweden, SGI Report No. 17, pp. 423–454.

Thakur, V. 2016. Landslide hazards in sensitive clays: Recent advances in assessment and mitigation strategies. *In* Proceedings of the 17th Nordic Geotechnical Meeting Challenges in Nordic Geotechnic, NGM 2016 Reykjavik, pp. 1141–1152.

Thakur, V., Degago, S.A., Selänpää, J., and Länsivaara, T. 2017. Determination of remoulding energy of sensitive clays. *In* Landslides in Sensitive Clays, From Research to Implementation, Advances in Natural and Technological Hazards Research, Volume 46, Springer, V. Thakur et al. (eds.), pp. 97–107.

Thakur, V., and Degago, S.A. 2014. Identification of sensitive clays susceptible to flow slides using remolding energy concept. *In* Proceedings of the Computer Methods and Recent Advances in Geomechanics, F. Oka, S. Kimoto, R. Uzuoka and A. Murakami (ed.), Kyoto, Japan, pp. 1–6.

Thakur, V., Nordal, S., Viggiani, G., and Charrier, P. 2018. Shear bands in undrained plane strain compression of Norwegian quick clays. Can. Geotech. J. **55**: 45–56.

Theenathayarl, T. 2015. Behaviour of sensitive Leda clay under simple shear loading, Ph.D. thesis, Carleton University, Ottawa, Canada.

Trapper, P. A., Puzrin, A. M., and Germanovich, L. N. 2015. Effects of shear band propagation on early waves generated by initial breakoff of tsunamigenic landslides. Marine Geology, **370**: 99–112.

Tsai, C. C., Park, D., and Chen, C. W. 2014. Selection of the optimal frequencies of viscous damping formulation in nonlinear time-domain site response analysis. Soil Dynamics and Earthquake Engineering, **67**: 353–358.

Villaverde, R. 2009. Fundamental concepts of earthquake engineering. CRC Press.

Wang, C., and Hawlader, B. 2017. Numerical modeling of three types of sensitive clay slope failures. *In* Proceedings of the 19th International Conference on Soil Mechanics and Geotechnical Engineering, Seoul, South Korea, pp. 871–874.

Wang, D., Randolph, M. F., and White, D. J. 2013. A dynamic large deformation finite element method based on mesh regeneration. Computers and Geotechnics, **54**: 192–201.

Wang, C., Saha, B., and Hawlader, B. 2015. Some factors affecting retrogressive failure of sensitive clay slopes using large deformation finite element modeling. *In* 68th Canadian Geotechnical Conference and the 7th Canadian Permafrost Conference, Quebec City, Canada, Sept 21–23, pp. 1-6.

Wartman, J. 1999. Physical model studies of seismically induced deformation in slopes. Ph.D. thesis, The University of California, Berkeley, USA.

Wartman, J., Seed, R. B., and Bray, J. D. 2005. Shaking table modeling of seismically induced deformations in slopes. Journal of Geotechnical and Geoenvironmental Engineering. **131**(5): 610–622.

Wetmiller, R. J., Horner, R. B., Hasegawa, H. S., North, R. G., Lamontagne, M., Weichert, D. H., and Evans, S. G. 1998. An analysis of the 1985 Nahanni earthquakes, Bulletin of the Seismological Society of America, **78**(2): 590–616.

Woodward-Clyde 1982. Anchorage Office Complex, Geotechnical Investigation, Anchorage, Alaska.

Zhai, E., Roth, W., Dawson, E., and Davis, C. 2004. Seismic deformation analysis of an earth dam—a comparison study between equivalent-linear and nonlinear effective-stress approaches. *In* Proceedings of the 13th world conference on earthquake engineering, Vancouver, BC, Canada, pp. 1–6.

Zhang, W., Wang, D., Randolph, M.F., and Puzrin, A.M. 2015. Catastrophic failure in planar landslides with a fully softened weak zone. Géotechnique, **65**(9): 755–769

Zhou, H., and Randolph, M. F. 2009. Numerical investigations into cycling of full-flow penetrometers in soft clay. Géotechnique, **59**(10): 801–812.

Table 1. Geotechnical parameters used for base case analysis

Parameters	Value			
	Sensitive Clay	Stiff Clay	Base	Highly sensitive Clay (Slope-IV)
Undrained Young's Modulus, E_u (MPa)	10	10	100	10
Poisson's ratio, ν_u	0.495	0.495	0.495	0.495
Peak undrained shear strength, s_{u0} (kPa)	Linear§	Linear§	—	55
Remoulded undrained shear strength, s_{uR} (kPa)	$s_{u0}/3.5$	s_{u0}	—	$s_{u0}/30$
Large displacement undrained shear strength, s_{uld} (kPa)	$s_{u0}/16$	s_{u0}	—	$s_{u0}/50$
Plastic shear displacement for initiation of softening, δ_{pc} (m)*	0.006	—	—	0.006
Plastic shear displacement for 95% degradation of soil strength, δ_{95} (m)	0.035	—	—	0.01
Plastic shear displacement for large displacement undrained shear strength, δ_{ld} (m)	2	—	—	2
Saturated unit weight of soil, γ_{sat} (kN/m^3)	20	20	20	20
Rayleigh damping parameter, β	0.000375	0.000375	-	0.000375

§ s_{u0} varies linearly with depth below the crest of the slope (z) as s_{u0} (in kPa)=25+2z (in m)

* for FE input, the plastic shear strain is calculated using δ and thickness of finite element

Table 2. Effects of strain-softening parameters on failure of Slope-I

Case #	s_{u0}/s_{uR}	δ_{95} (m)	$s_{u0}/s_{u(ld)}$	δ_{ld} (m)	E_R (kN-m/m^3)	E_k (kN-m/m^3)	L_{umax} (m)	L_{Rmax} (m)	Retrogression pattern
I	3.5	0.035	3.5	2.0	96	104	44	49	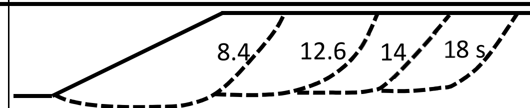
II	3.5	0.035	8	2.0	73	127	79	51	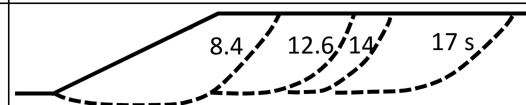
III	3.5	0.035	16	2.0	60	140	120	61	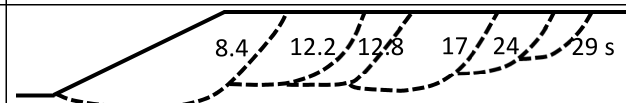
IV	3.5	0.035	16	0.5	18	182	129	63	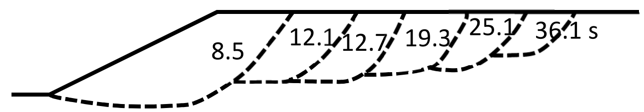
V	3.5	0.035	50	0.5	16	184	189	79	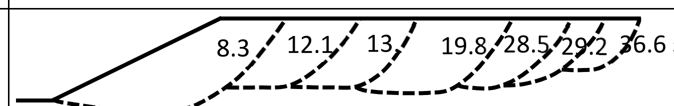
VI	3.5	0.035	50	0.25	10	190	196	58	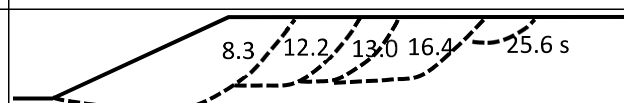
VII	6	0.035	16	2.0	40	160	170	138	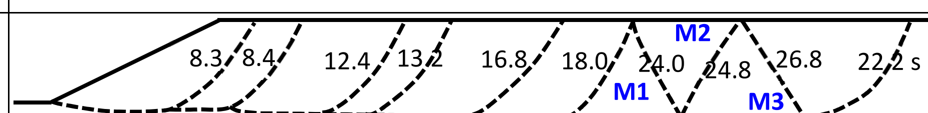

VIII	9	0.035	16	2.0	31	169	182	112	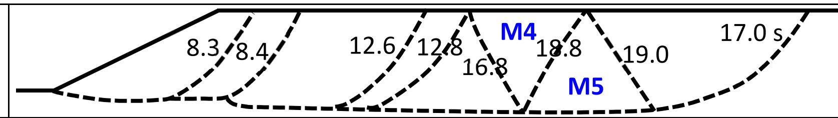
IX	3.5	0.07	16	2.0	62	138	95	43	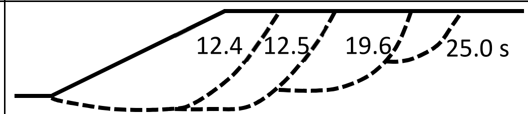
X	3.5	0.15	16	2.0	94	107	81	36	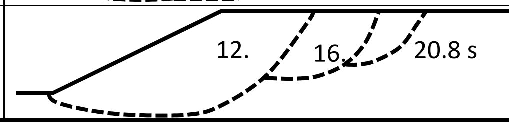

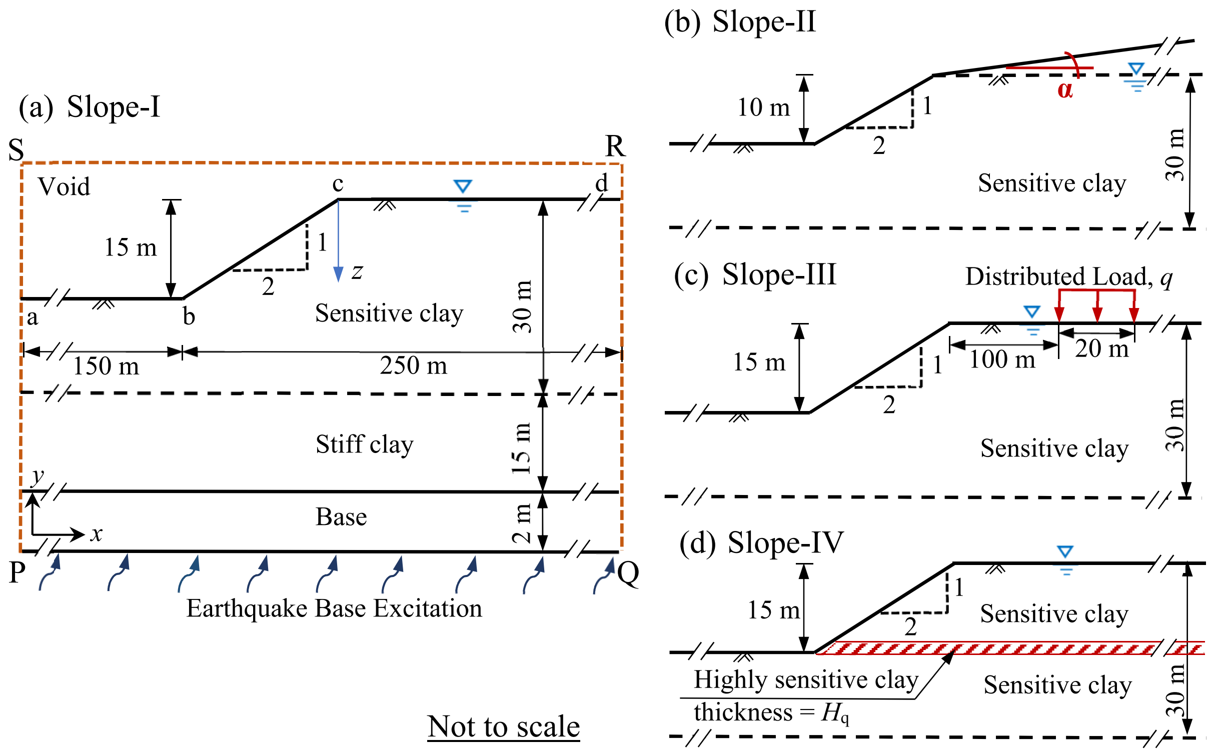

Fig. 1. Model geometries: (a) Slope-I, horizontal ground surface; (b) Slope-II, slightly inclined upslope ground surface; (c) Slope-III, with upslope distributed load, and (d) Slope-IV, highly sensitive clay layer at toe depth

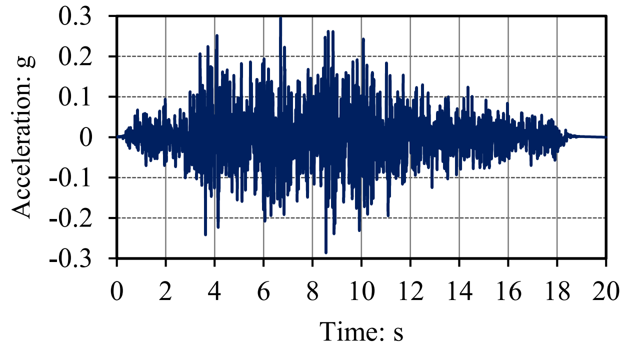

Fig. 2. Acceleration–time history used in finite-element analysis (modified from 1985 Nahanni earthquake)

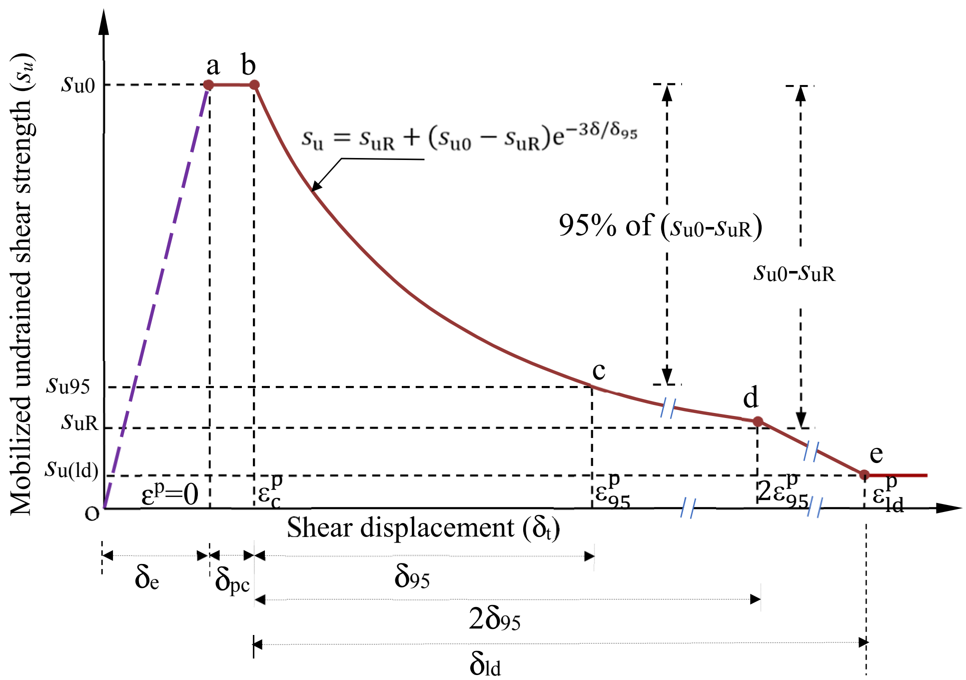

Fig. 3. Stress–strain behaviour used in finite-element modeling (after Dey et al., 2015)

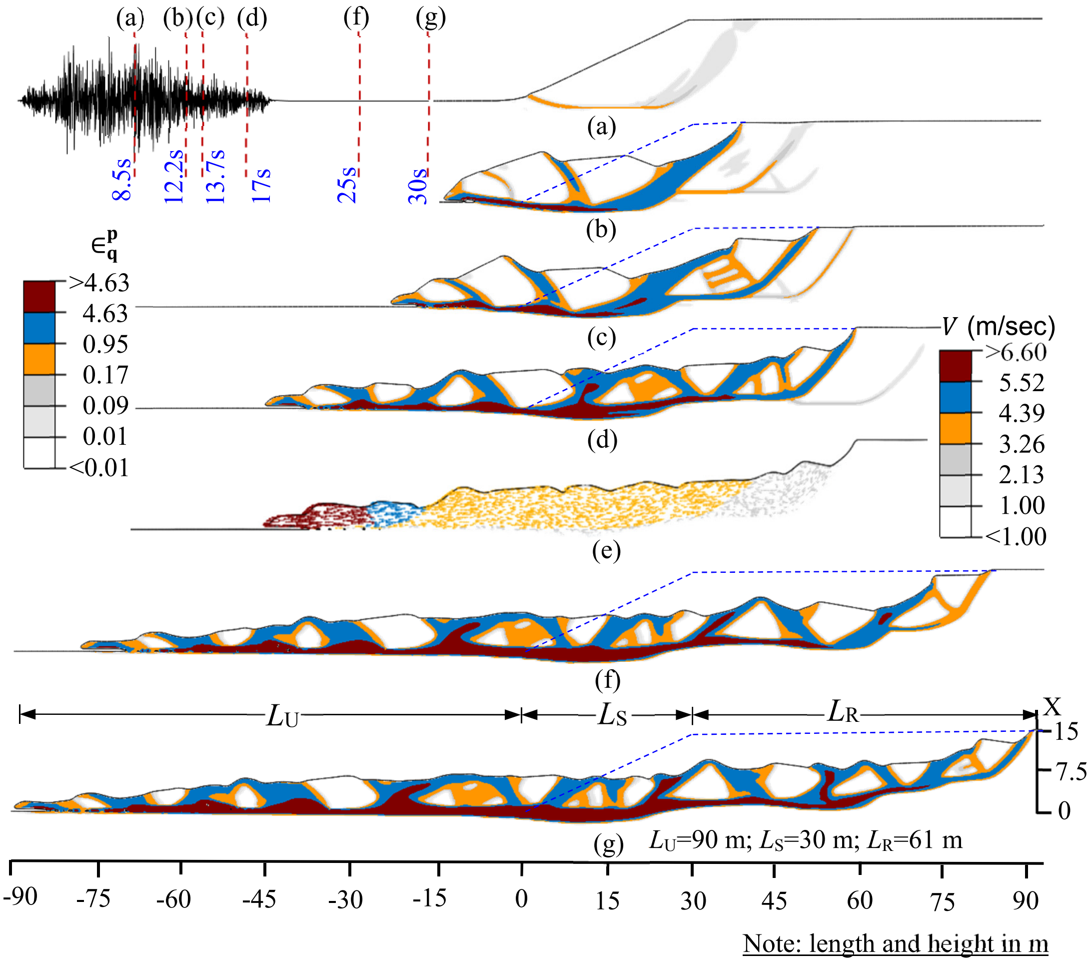

Fig. 4. Formation of failure planes in Slope-I

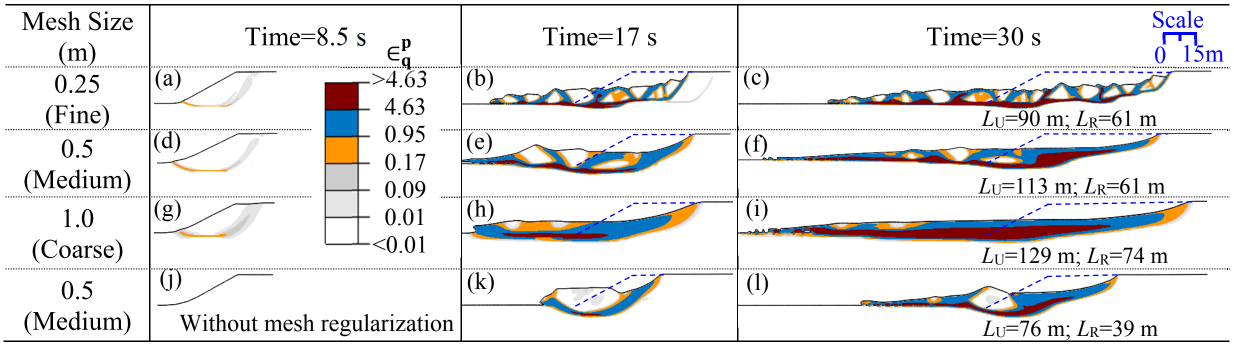

Fig. 5. Effect of FE mesh size on the formation of failure planes in Slope-I

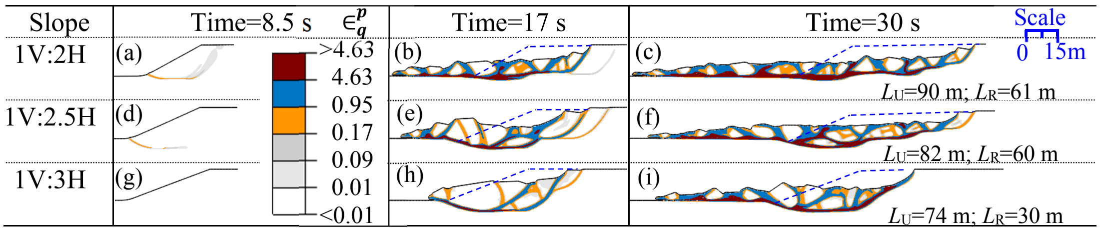

Fig. 6. Effect of slope inclination on failure of Slope-I

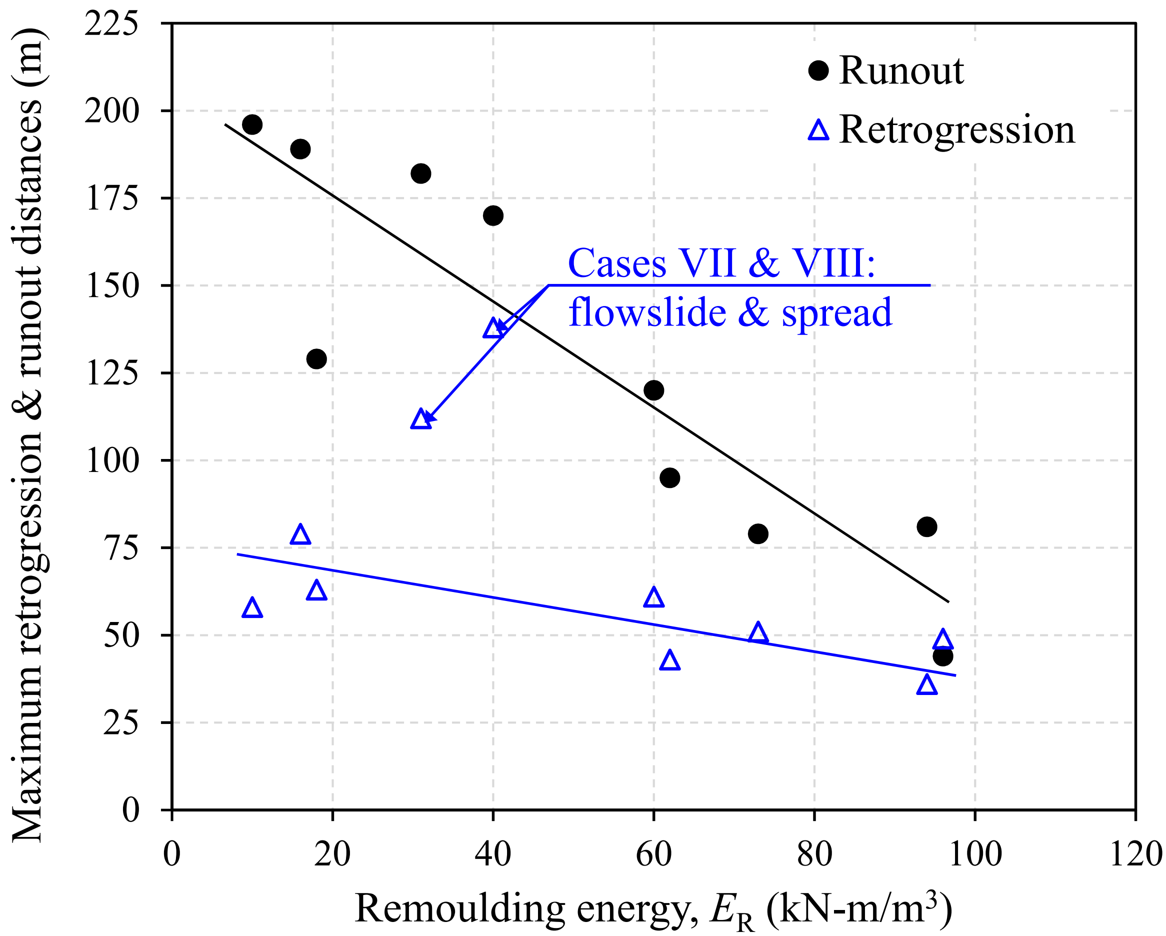

Fig. 7. Effects of post-peak softening on maximum retrogression and runout distances for Slope-I: (a) effects of remoulding energy

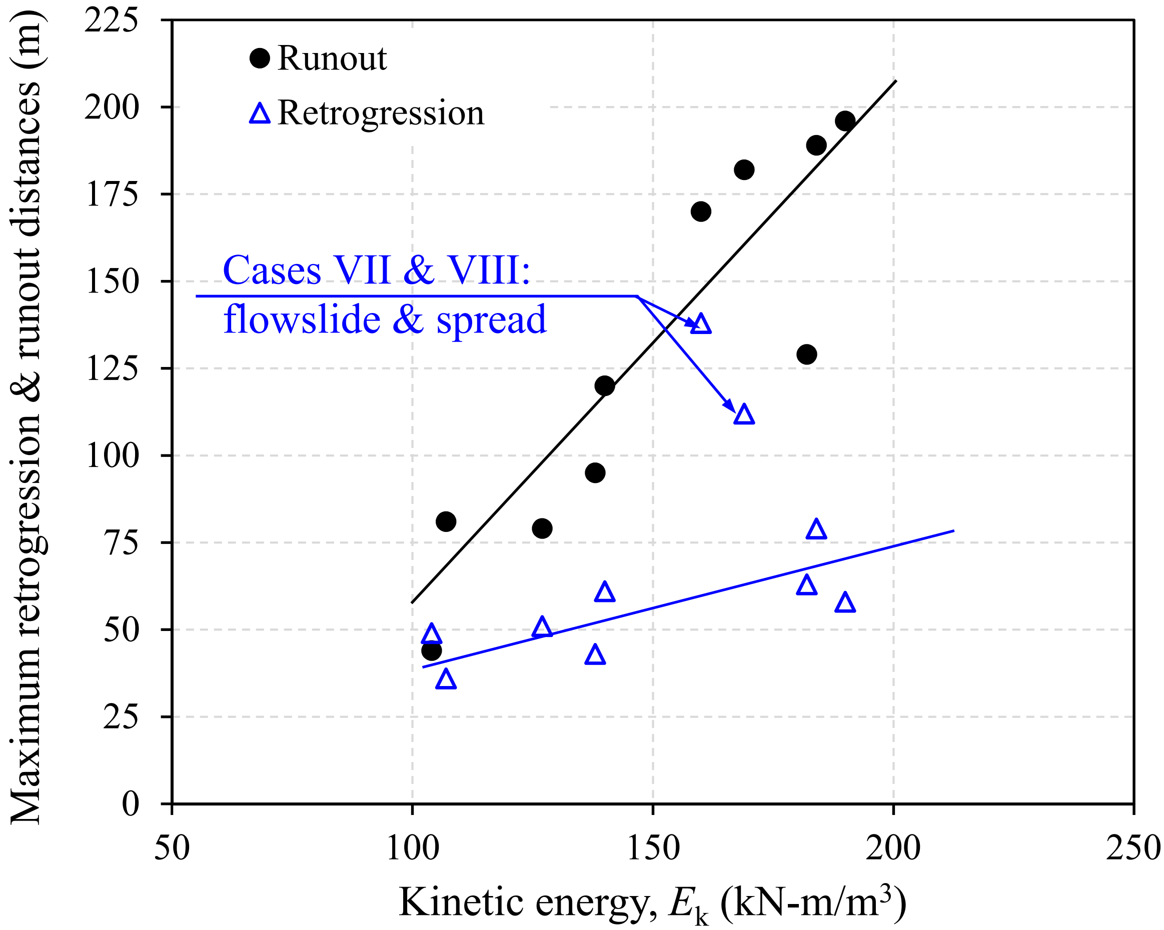

Fig. 7. Effects of post-peak softening on maximum retrogression and runout distances for Slope-I: (b) effects of kinetic energy

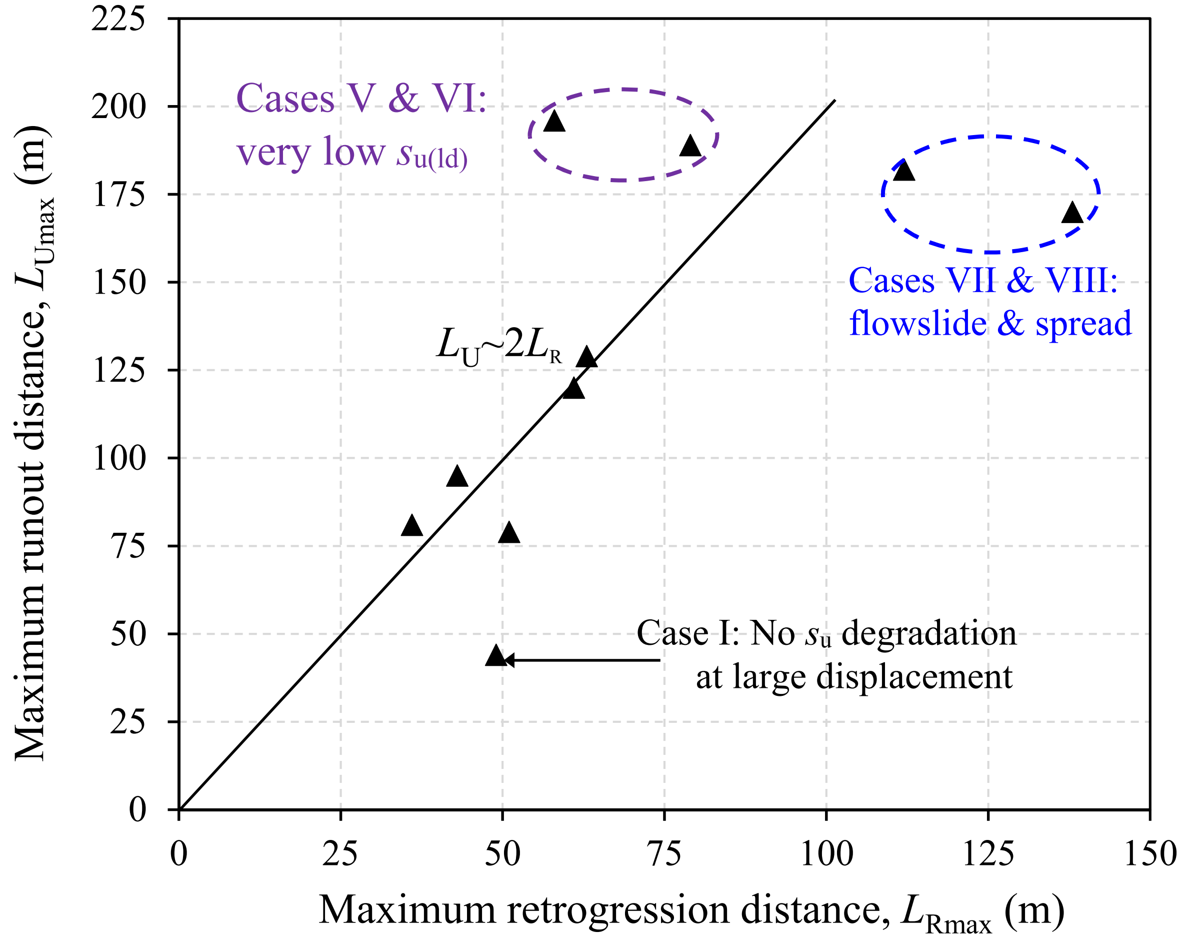

Fig. 7. Effects of post-peak softening on maximum retrogression and runout distances for Slope-I: (c) relation between retrogression and runout

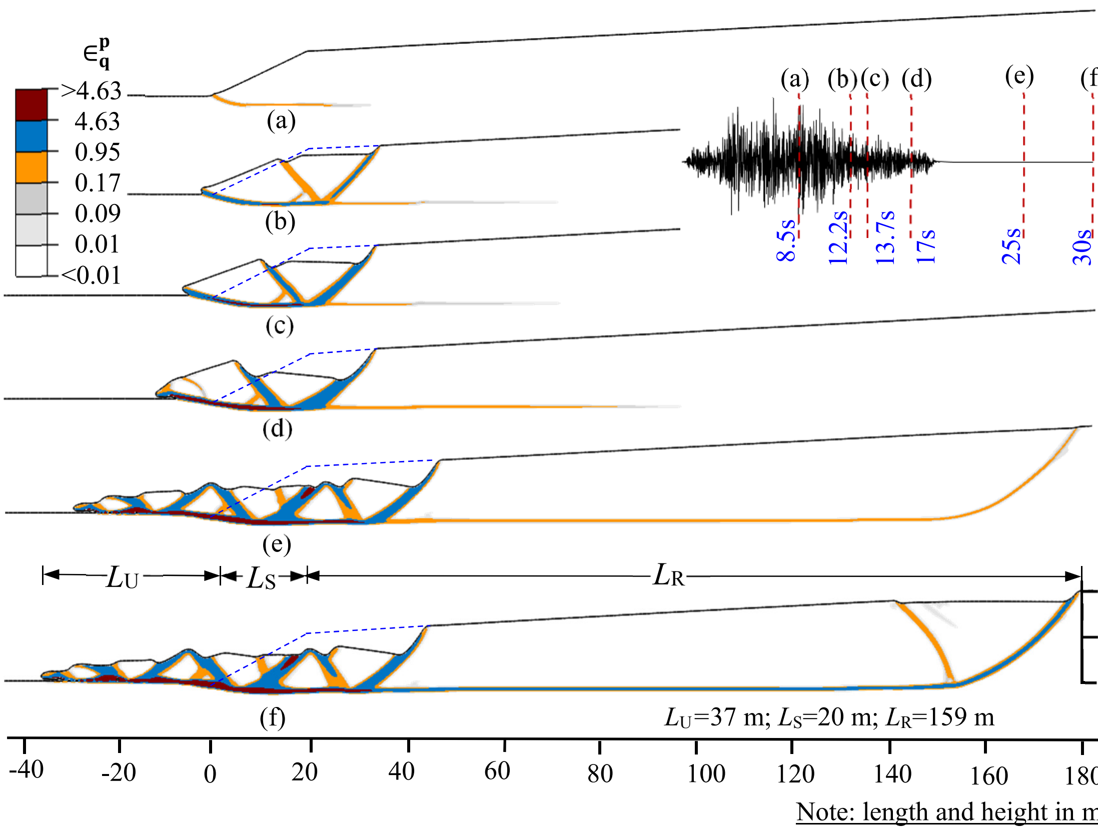

Fig. 8. Formation of failure planes in Slope-II

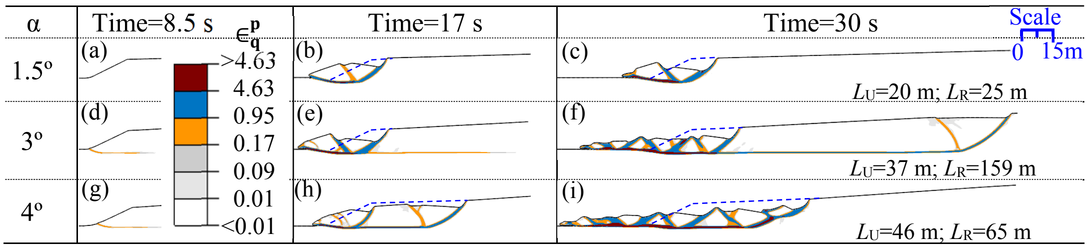

Fig. 9. Effect of upslope inclination on failure of Slope-II

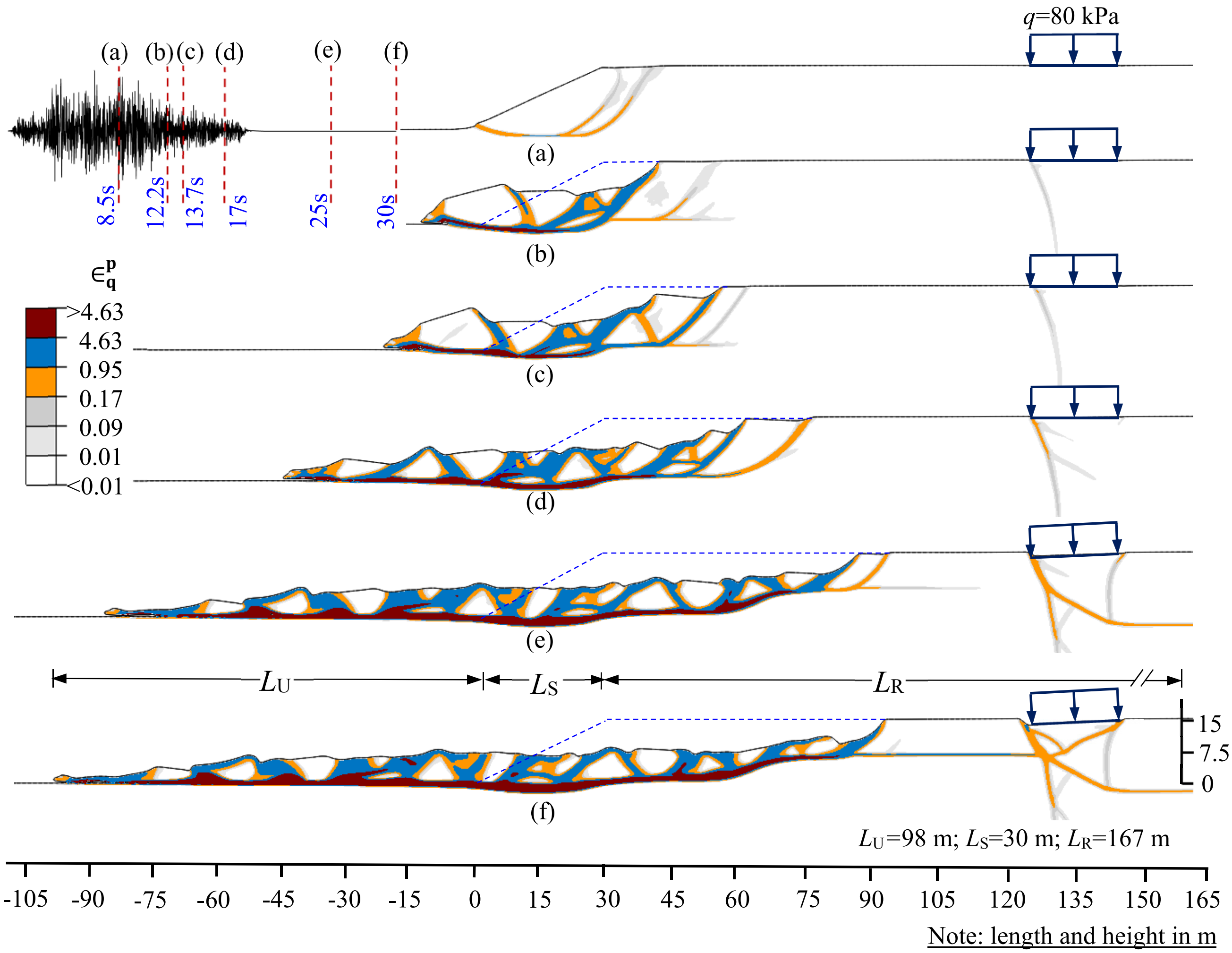

Fig. 10. Formation of failure planes in Slope-III

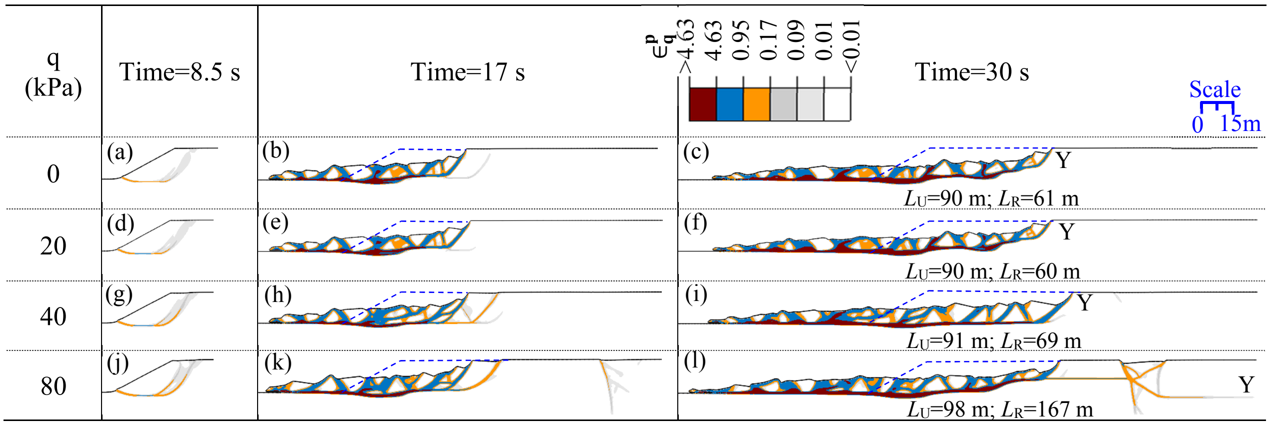

Fig. 11. Effect of distributed loads on failure of Slope-III

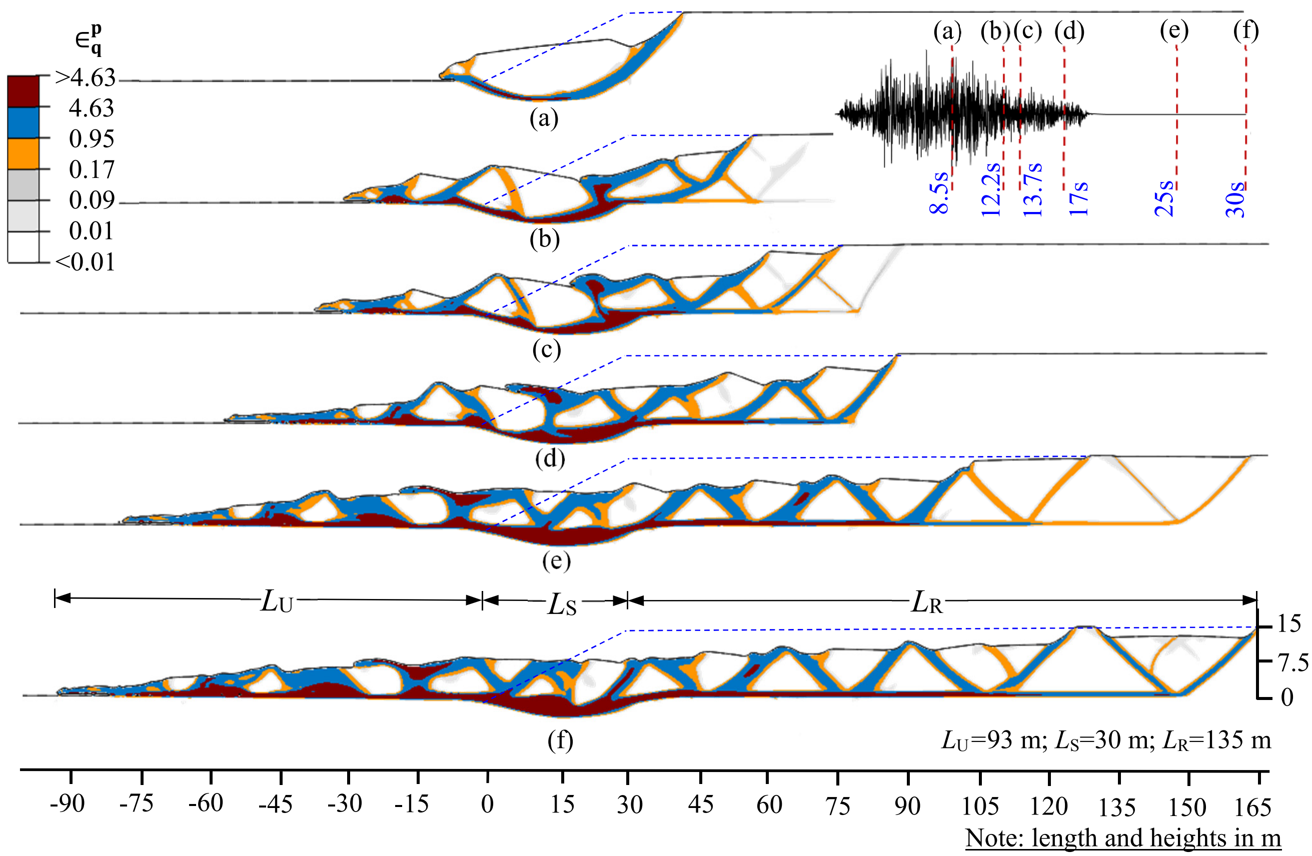

Fig. 12. Formation of failure planes in Slope-IV

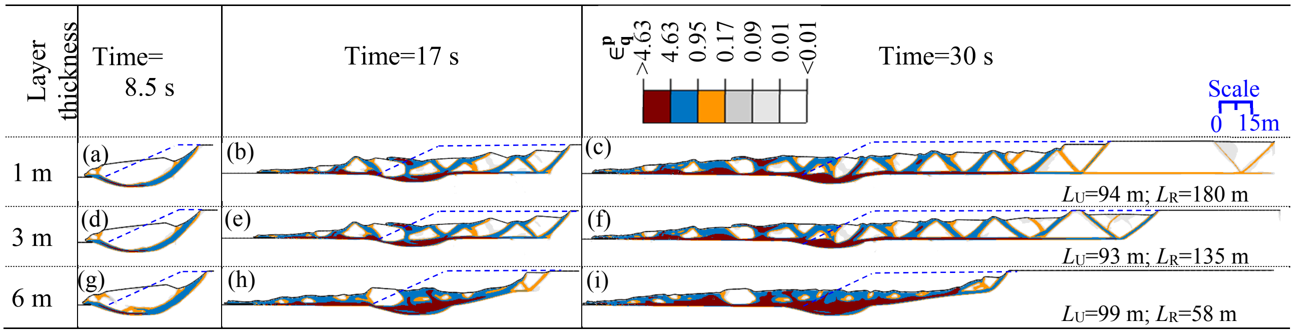

Fig. 13. Effect of change in highly sensitive clay layer thickness on failure of Slope-IV